scientific reports

Check for updates

OPEN

2'-Nitroflavone targets PARP1 and alters cytoskeleton to inhibit triple-negative breast cancer progression

Vanina S. Vachetta[1,2], Viviana C. Blank[1,2], Mariel Marder[1,2], Melisa B. Nicoud[3,4], Jorge Cantero[5,6], Miriam Benso[1,2], Silvia Vanzulli[7], María G. Ortega[8], Margot Paulino Zunini[5], Vanina A. Medina[3,4], María T. Elola[1,2,9] & María F. Troncoso[1,2,9]✉

Triple-negative breast cancer (TNBC) is an aggressive subtype, often resistant to chemotherapy. Flavonoids are polyphenolic compounds that exhibit anticancer properties. In this study, the potential antitumor effects of the synthetic flavonoid 2′-nitroflavone (2'NF) in TNBC were investigated. Our in vitro results show that 2′NF reduces TNBC cell viability, proliferation, and survival, while inducing cell cycle arrest, apoptosis, and mitotic catastrophe. Additionally, 2'NF inhibits TNBC and endothelial cell migration, likely due to severe disruptions in tubulin and actin cytoskeletons. Computational analysis revealed that 2′NF has a favorable pharmacological profile as a potential drug candidate. In a murine TNBC model, 2'NF administration slowed tumor growth without evident toxicity. Mechanistic in silico studies propose that poly(ADP-ribose) polymerase-1 (PARP1), a key enzyme involved in DNA repair, may be a target of 2′NF. Molecular docking and dynamics simulations demonstrated the formation of a thermodynamically stable complex between 2′NF and the catalytic domain of PARP1. Moreover, in vitro PARP enzymatic activity was inhibited by 2′NF in TNBC cells. These promising findings suggest the potential of 2′NF as a novel PARP1 inhibitor or a scaffold for developing improved inhibitors, offering new avenues for combination therapies in TNBC treatment.

Keywords Flavonoid, Triple-negative breast cancer, Apoptosis, Mitotic catastrophe, Cytoskeleton alterations, PARP1 interaction

Abbreviations

ADME	Absorption, distribution, metabolism, and excretion
AhR	Aryl hydrocarbon receptor
AO	Acridine orange
AR	Androgen receptor
BRCA1/2	Breast cancer type 1 and type 2 genes
CM	Conditioned media
DABCO	1,4-Diazabiciclo[2.2.2]octano
DAPI	4',6-Diamidino-2-phenylindole
DMSO	Dimethyl sulfoxide
EB	Ethidium bromide

[1]Departamento de Química Biológica, Facultad de Farmacia y Bioquímica, Universidad de Buenos Aires, Buenos Aires, Argentina. [2]Consejo Nacional de Investigaciones Científicas y Técnicas (CONICET), Instituto de Química y Fisicoquímica Biológicas (IQUIFIB) Prof. Alejandro C. Paladini, Universidad de Buenos Aires, Buenos Aires, Argentina. [3]Departamento de Fisicomatemática, Facultad de Farmacia y Bioquímica, Universidad de Buenos Aires, Buenos Aires, Argentina. [4]Laboratorio de Biología Tumoral e Inflamación, Facultad de Ciencias Médicas, Instituto de Investigaciones Biomédicas (BIOMED), Consejo Nacional de Investigaciones Científicas y Técnicas (CONICET), Pontificia Universidad Católica Argentina (UCA), 1107 Buenos Aires, Argentina. [5]Centro de Bioinformática, Facultad de Química, Universidad de la República, Montevideo, Uruguay. [6]Centro de Investigaciones Médicas, Facultad de Ciencias de la Salud, Universidad Nacional del Este, Ciudad del Este, Paraguay. [7]Instituto de Investigaciones Hematológicas (IIHEMA), Academia Nacional De Medicina, Buenos Aires, Argentina. [8]Farmacognosia, Departamento de Ciencias Farmacéuticas, Facultad de Ciencias Químicas, Universidad Nacional de Córdoba, Instituto Multidisciplinario de Biología Vegetal (IMBIV-CONICET), Ciudad Universitaria, Córdoba, Argentina. [9]María T. Elola and María F. Troncoso contributed equally to this work. ✉email: mf.troncoso@ffyb.uba.ar; ma.f.troncoso@gmail.com

ECL	Chemiluminescence
EGCG	Epigallocatechin-3-gallate
ER α/β	Estrogen receptor α/β
FBS	Fetal bovine serum
HER2	Human epidermal growth factor receptor 2
HRP	Horseradish-peroxidase
HRR	Homologous recombination repair
IC_{50}	Maximal inhibitory concentration 50
MD	Molecular dynamics
MOE	Molecular operating environment
MTT	3-[4,5-Dimethylthiazol-2-yl]-2,5-diphenyltetrazolium bromide
2'NF	2'-Nitroflavone
PAINS	Pan-assay interference compounds
PAR	Poly(ADP-ribose) polymers
PARP1	Poly(ADP-ribose) polymerase 1
PARPi	PARP inhibitors
PASS	Prediction of activity spectra for substances
PEG	Polyethileneglycol
PI	Propidium iodide
PLIF	Protein ligand interaction fingerprint
PR	Progesterone receptor
PTEN	Phosphatase and tensin homolog deleted on chromosome ten
QSAR	Quantitative structure-activity relationships
RMSD	Root-mean-square deviation
RMSF	Root-mean-square fluctuation
SEA	Similarity ensemble approach
SEM	Standard error of the mean
SL	Synthetic lethality
TNKS	Tankyrase
TNBC	Triple-negative breast cancer
TRITC	Tetramethylrhodamine isothiocyanate
VEGFA	Vascular endothelial growth factor A

Triple-negative breast cancer (TNBC) refers to mammary gland tumors that lack expression of the estrogen receptor (ER), progesterone receptor (PR) and human epidermal growth factor receptor 2 (HER2)[1–3]. It accounts for approximately 15–20% of all breast cancers[4]. Patients with TNBC typically have a poor prognosis due to unfavorable characteristics such as high histological grade, metastasis and large tumor size, further complicated by highly heterogeneous gene profiles[5–7]. As neither hormonal nor anti-HER2 therapies are suitable, treatment relies on conventional approaches such as surgery, chemotherapy, radiotherapy and immunotherapy. However, chemotherapy often causes severe side effects, chemoresistance and the enrichment in cancer stem cells, promoting tumorigenesis and relapse[8]. Other targeted agents, including bevacizumab (anti-angiogenic) and sunitinib (multi-kinase inhibitor), have also failed to show significant clinical benefit[9]. In immunotherapy, despite advances in next-generation strategies, current options remain largely restricted to immune checkpoint inhibitors combined with chemotherapy[10]. Consequently, there is a continuous search for new therapeutic options.

In this context, a diverse class of chemical compounds derived from plants could provide novel alternative treatments to avoid multidrug chemoresistance in TNBC. For example, sulforaphane, curcumin, resveratrol and lycopene are promising phytochemicals for TNBC treatment[8,11]. Among natural products, flavonoids, a large group of polyphenols with low molecular weight found in nearly all fruits and vegetables[12], have gained attention. Flavonoids exert numerous biological effects on different cell types by influencing growth through mechanisms such as cell cycle arrest, apoptosis and necrosis. Additionally, they exhibit antitumor properties but also other multiple bioactivities such as drug resistance reduction, cardiovascular protective effects, nerve system protective effects, anti-aging and anti-inflammatory functions, which convert them in good candidates to mitigate chemotherapy-related side effects in cancer patients in combined therapies with conventional chemotherapeutics[13–16].

Some well-studied flavonoids such as genistein, kaempferol, luteolin and epigallocatechin-3-gallate (EGCG) seem to have the strongest evidence in treating TNBC[8,11]. Several flavonoids specifically affect cell cycle progression and proliferation, leading to apoptosis[17]. For instance, genistein induces cell cycle arrest in the G2/M phase and inhibits proliferation by triggering apoptosis in human TNBC MDA-MB-231 cells[18]. Similarly, eupatorin induces apoptosis while inhibiting invasion, migration and angiogenesis in MDA-MB-231 cells by blocking the phospho-AKT pathway and arresting the cell cycle[19]. Calycopterin also reduces proliferation and colony formation, increases cell population at sub-G1 (hypodiploid) phase and induces apoptosis in MDA-MB-231 cells[20].

Notably, the synthetic flavonoid 2'-nitroflavone (2'NF) (Fig. 1) has demonstrated significant effects in inducing apoptosis in various cancer models. Previous studies showed that treatment with 2'NF in HeLa cervix adenocarcinoma and HL60 leukemia human cells induced apoptosis, characterized by increased sub-G1 cell percentages, chromatin condensation, membrane blebbing and the typical DNA ladder fragmentation. This apoptosis was regulated by caspase-8 and -9, with activation of the death receptor pathway (extrinsic apoptosis) and release of cytochrome C into the cytosol (intrinsic apoptosis), respectively[21,22]. In $HER2^+$ subtype LM3

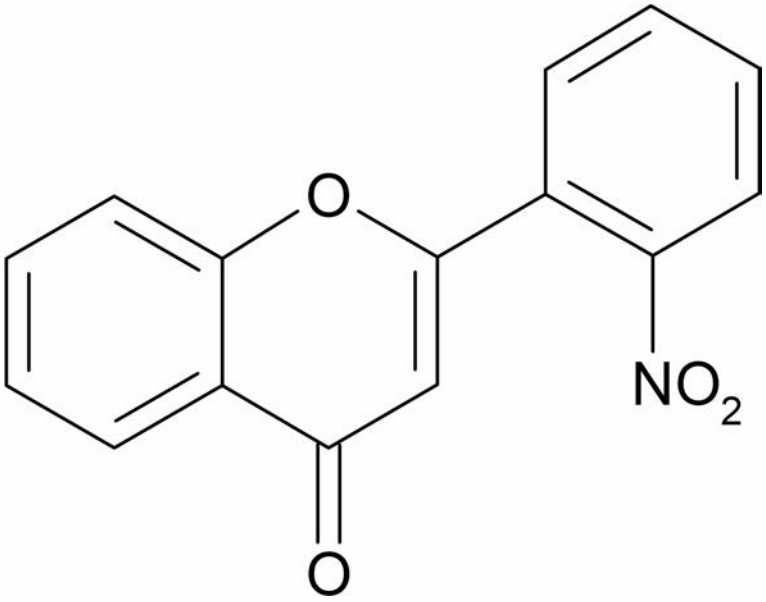

Fig. 1. Chemical structure of 2'NF represented in two dimensions.

murine breast cancer cells, 2'NF increased hypodiploid cells, DNA ladder fragmentation, and activation of caspase-8, -9, and -3, along with elevated proapoptotic protein Bax and cytosolic cytochrome C levels. Importantly, in a BALB/c mouse model inoculated with syngeneic LM3 cells, intraperitoneal treatment with 2'NF significantly reduced tumor volume compared to the vehicle. No toxicity was observed in various organs of non-tumor-bearing mice[23]. Based on these previous findings, the translational potential of 2'NF in TNBC patients appears promising, particularly in view of the persistent limitations of current treatments, including side effects and chemoresistance to conventional chemotherapeutics. Therefore, in this study, we evaluated the cytotoxic effects of 2'NF on different TNBC cell lines and investigated the underlying mechanisms.

Results

2'NF inhibits viability, proliferation, survival and impairs cell cycle progression of TNBC cells

First, we evaluated the 2'NF effect on human TNBC cell viability, which was assessed by the MTT assay and plotted versus 2'NF concentration on dose–response curves for different times. 2'NF inhibited MDA-MB-231 (mesenchymal stem-like TNBC subtype), BT-549 (mesenchymal TNBC subtype) and MDA-MB-468 (basal-like TNBC subtype)[5] cell viability (Fig. 2a). In MDA-MB-231 cells, the curve reached a plateau at 48 and 72 h at a concentration of 10 μM, while in BT-549 cells, the same occurred at 20 μM. In MDA-MB-468 cells, the decrease in viability was greater than in the other two cell lines. Half maximal inhibitory concentration (IC_{50}) values ranged from 4 to 9.2 μM after 72 h for all TNBC cells (Fig. 2b). After performing trypan blue exclusion assay, an antiproliferative response was observed in 2´NF-treated cells at 72 h (Fig. 2c). Next, 2'NF effect on clonogenic TNBC cell survival potential was determined. Significant inhibitory effects on colony formation were observed in 2'NF-treated TNBC cells after 72 or 144 h (Fig. 2d). Moreover, cell cycle analysis revealed that 2'NF (5 μM) induced S and G2/M arrest in MDA-MB-231 cells after 72 h-treatment (Fig. 2e).

2'NF induces apoptosis and mitotic catastrophe in TNBC cells

To investigate if the flavonoid induces apoptosis on TNBC cells, MDA-MB-231 cells were incubated with 2'NF for 72 h. Acridine orange/ethidium bromide staining followed by fluorescence microscopy analysis showed that 2'NF at 25 μM significantly decreased viable cells and increased the percentage of early apoptotic cells (Fig. 3a). Apoptosis induction was further confirmed by propidium iodide (PI) staining and flow cytometry analysis (Fig. 3b), and Western blotting detection of PARP1 cleavage (Fig. 3c). 2'NF at 5 and 25 μM significantly increased the percentage of hypodiploid cells and induced PARP1 cleavage (Fig. 3b and c). Furthermore, TRITC-phalloidin and DAPI staining revealed that 2'NF (25 μM) produced giant multinucleated MDA-MB-231 and BT-549 cells (Fig. 3d), a morphological marker of mitotic catastrophe.

2'NF decreases TNBC cell migration

Wound-healing assays were conducted to assess 2'NF effect on TNBC cell migration. Under conditions in which neither cell viability nor proliferation were affected (Fig.S1), 2'NF inhibited MDA-MB-231 and BT-549 cell migration in a dose-dependent manner in the absence of fetal bovine serum (FBS) (Fig. 4a and b). Conversely, the flavonoid had no effect on MDA-MB-468 cell migration (Fig. 4a and b); however, these cells significantly proliferated even in the absence of FBS during cell migration assays (Fig. S1), implying that wound closure observed in these experiments was promoted by a combined effect on cell migration and proliferation.

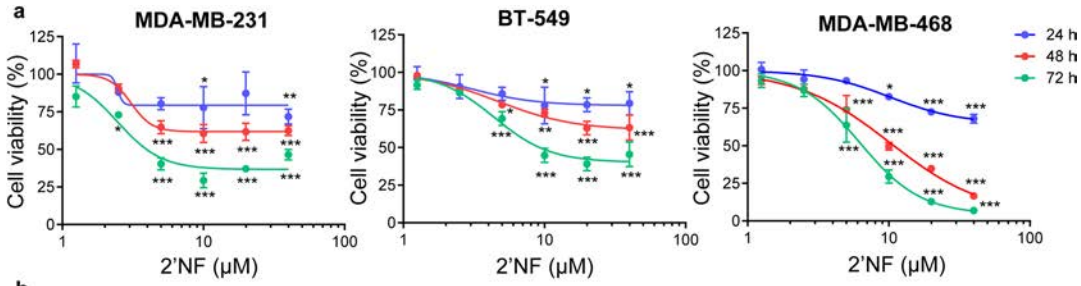

b

2'NF treatment (h)	IC_{50} (95% CI) (μM)		
	MDA-MB-231	BT-549	MDA-MB-468
72	4.0 (2.9-6.1)	9.2 (6.5-15.4)	6.5 (5.4-7.9)

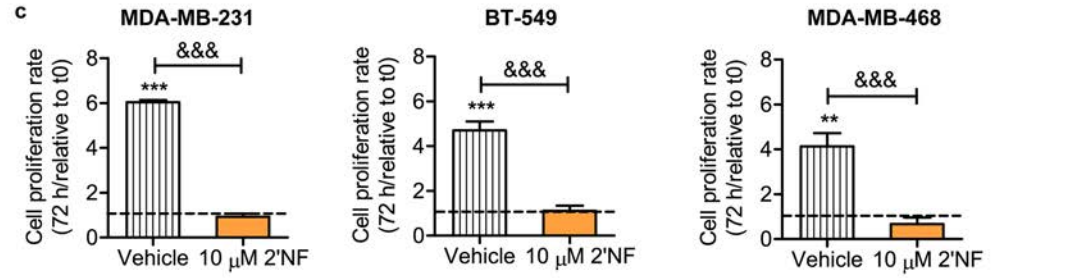

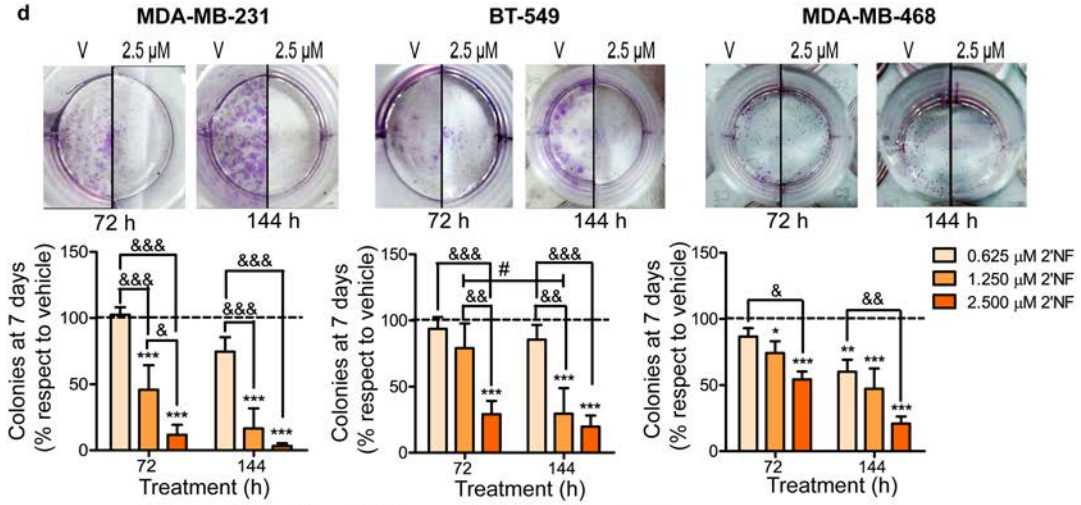

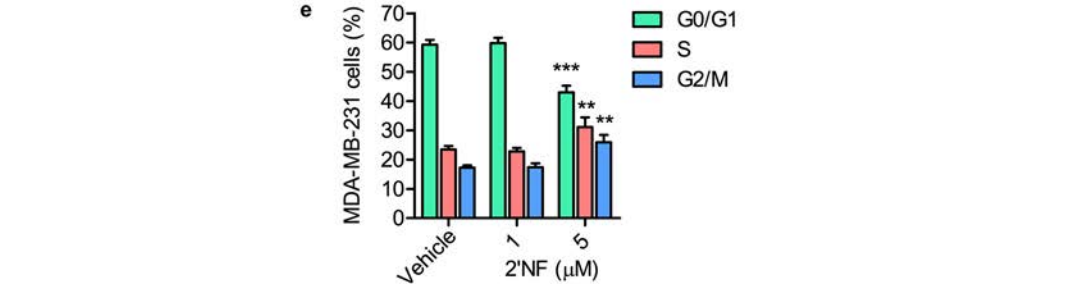

2'NF alters α-tubulin and actin cytoskeleton on TNBC cells

Considering the fundamental role of microtubules and actin filaments in cell division[24,25] and migration, we next investigated 2'NF effect on α-tubulin and actin cytoskeleton in TNBC cells. In both MDA-MB-231 and BT-549 cells, 72 h-treatment with 25 μM 2'NF significantly decreased α-tubulin protein expression, while actin protein levels were not affected at any of the concentrations tested (Fig. 5a). Moreover, acetylated α-tubulin levels increased in MDA-MB-231 cells incubated with the flavonoid (25 μM) (Fig. 5b). In immunofluorescence assays, most of vehicle-treated cells showed a high-density focus of α-tubulin close to the nucleus (Fig. 5c and d). This pattern may be the typical radial organization of microtubules which emanate from the centrosome, probably constituting the nuclear microtubule-organizing center (MTOC). In contrast, most cells treated with 2'NF showed a decrease in α-tubulin density close to the nucleus (Fig. 5c and d). Remarkably, multipolar spindles were found in both MDA-MB-231 and BT-549 cells after treatment with the flavonoid, which were not

◀**Fig. 2**. The flavonoid 2'NF inhibits viability, proliferation, survival and impairs cell cycle progression of TNBC cells. (**a**) Viability of MDA-MB-231, BT-549 and MDA-MB-468 cells was evaluated after treatment with 2'NF or vehicle using the MTT assay. Results correspond to mean ± SEM (n = 3–5 independent experiments). Significant differences respect to vehicle (100%) were determined using two-way ANOVA followed by Bonferroni´s post-test. $^{*}p < 0.05$; $^{**}p < 0.01$; $^{***}p < 0.001$. (**b**) 2'NF half-maximal inhibitory concentration (IC_{50}) values were obtained from dose–response viability curves after 72 h-treatment for each cell line using GraphPad Prism software. CI: confidence interval. (**c**) Proliferation rate of TNBC cells was quantified after treatment with 10 μM 2'NF or vehicle for 72 h using trypan blue dye exclusion assay. Cell counting was performed at the beginning of the treatment (0 h, taken as 1; dashed line) and after 72 h. Results correspond to mean ± SEM (n = 3–4 independent experiments); one-way ANOVA followed by Bonferroni´s post-test. $^{**}p < 0.01$; $^{***}p < 0.001$; $^{\&\&\&}p < 0.001$. (**d**) Anchorage-dependent colony formation evaluated in TNBC cells after treatment with 2'NF (0.625, 1.25 and 2.5 μM) or vehicle for 72 and 144 h. Upper panel: representative microphotographs. Magnification: ×1. Lower panel: results corresponding to mean ± SEM (n = 3–10 independent experiments); two-way ANOVA followed by Bonferroni´s post-test. $^{*}p < 0.05$; $^{**}p < 0.01$; $^{***}p < 0.001$, respect to vehicle (100%, dashed line). $^{\#}p < 0.05$ comparing 72 versus 144 h for a specific 2'NF concentration. $^{\&}p < 0.05$; $^{\&\&}p < 0.01$; $^{\&\&\&}p < 0.001$ comparing different 2'NF concentrations at a defined incubation time. (**e**) MDA-MB-231 cells were treated with 2'NF (1 and 5 μM) or vehicle for 72 h and then stained with propidium iodide and flow cytometry was performed. The percentage of cells in each phase of cell cycle was determined using Cylchred software. Results correspond to mean ± SEM (n = 4–8 independent experiments); one-way ANOVA followed by Dunnett´s post-test. $^{**}p < 0.01$; $^{***}p < 0.001$, respect to vehicle.

observed in cells incubated with vehicle (Fig. 5e). In fact, in the control condition, the characteristic bipolar spindle structure was found in dividing cells (Fig. 5e). Regarding the presence of actin filaments, F-actin staining with TRITC-phalloidin revealed that 2'NF (25 μM, 72 h) significantly decreased the percentage of BT-549 cells with actin stress fibers, respect to vehicle (Fig. 5f and g). These results indicate that 2'NF alters both tubulin and actin cytoskeleton.

2'NF reduces viability, migration and in vitro capillary-like tube formation of human endothelial cells

To find out 2'NF effects on endothelial cells, EA.hy926 cells were treated with 2'NF or cultured with conditioned media (CM) derived from TNBC cells pre-incubated with 2'NF. EA.hy926 cell viability was significantly reduced from 10 μM 2'NF after 96 h-treatment, rendering an IC_{50} of 14.5 μM (Fig. 6a). Importantly, endothelial cell migration after 24 h decreased in the presence of the flavonoid at a concentration of 1.25 μM (Fig. 6b), which did not reduce cell viability (Fig. S2). Interestingly, CM from 2´NF-treated MDA-MB-231 cells significantly decreased EA.hy926 cell viability (Fig. 6c), cell migration (Fig. 6d) and capillary-like tube formation (Fig. 5e and f). Moreover, in silico studies by PASS software predicted 2'NF activity as a *HIF1A* gene expression inhibitor (Supplementary Table 1). *HIF1A* encodes hypoxia-inducible factor 1-α (HIF-1α) transcription factor, which regulates the expression of genes involved in angiogenesis as part of the adaptation to hypoxia. Thus, these findings suggest potential anti-angiogenic effects of 2'NF on endothelial cells.

In silico drug-likeness of 2'NF

Molinspiration, SwissADME and admetSAR software were used to evaluate physicochemical properties, pharmacokinetics, drug-likeness and medicinal chemistry friendliness of 2'NF (Table 1). In silico predictions revealed that 2'NF does not violate the 'Lipinski´s rule of five' for drugs, has high gastrointestinal absorption and penetrates the blood–brain barrier. In turn, 2'NF would not act as a substrate for P-glycoprotein (P-gp), a transporter belonging to the ATP-binding cassette family, involved in drug efflux. Therefore, it has a favorable pharmacological profile as a drug candidate (Table 1).

2'NF reduces TNBC tumor volume in vivo

The antitumor effect of 2'NF in a $HER2^{+}$ breast cancer model using immunocompetent Balb/c mice had been previously demonstrated[23]. Based on our prediction that 2'NF could be a drug candidate, we next evaluated its effects in the syngeneic 4T1 TNBC model. First, we confirmed that 2'NF exerted a dose-dependent inhibitory effect on 4T1 cell viability in vitro (Fig. 7a and b). Then, mice were orthotopically injected with 4T1 cells and treated with the flavonoid (20 mg/kg) or vehicle. 2´NF-treated mice displayed significantly decreased relative tumor volume compared to control mice along the experiment (Fig. 7c). No statistical differences were observed in body, liver, spleen, heart and kidney weight between 2´NF-treated and vehicle mice (Fig. 7d–h), suggesting lack of in vivo 2'NF toxicity at the doses tested. Histopathological analysis in control tumors revealed increased extensive necrotic and hemorrhagic areas surrounded by interstitial edema and polymorphonuclear leukocyte infiltration such as it happens in rapidly growing tumors. However, minimal necrotic and hemorrhagic foci were observed in tumors from 2´NF-treated mice (Fig. 7i–p). These findings suggest that the reduction in tumor necrosis could be an indirect evidence of the decreased tumor growth induced by flavonoid.

2'NF in silico interacts with the catalytic domain of PARP1

Potential targets of 2'NF were predicted using the SwissTargetPrediction, TargetNet, Random Forest QSAR (Quantitative structure–activity relationships), SEA (Similarity ensemble approach) and SuperPred web servers, as well as the admetSAR software. Proteins were considered potential targets only if they were predicted by at least three of these tools (Table 2). Based on this analysis, potential interactions of 2'NF with PARP1, tankyrases

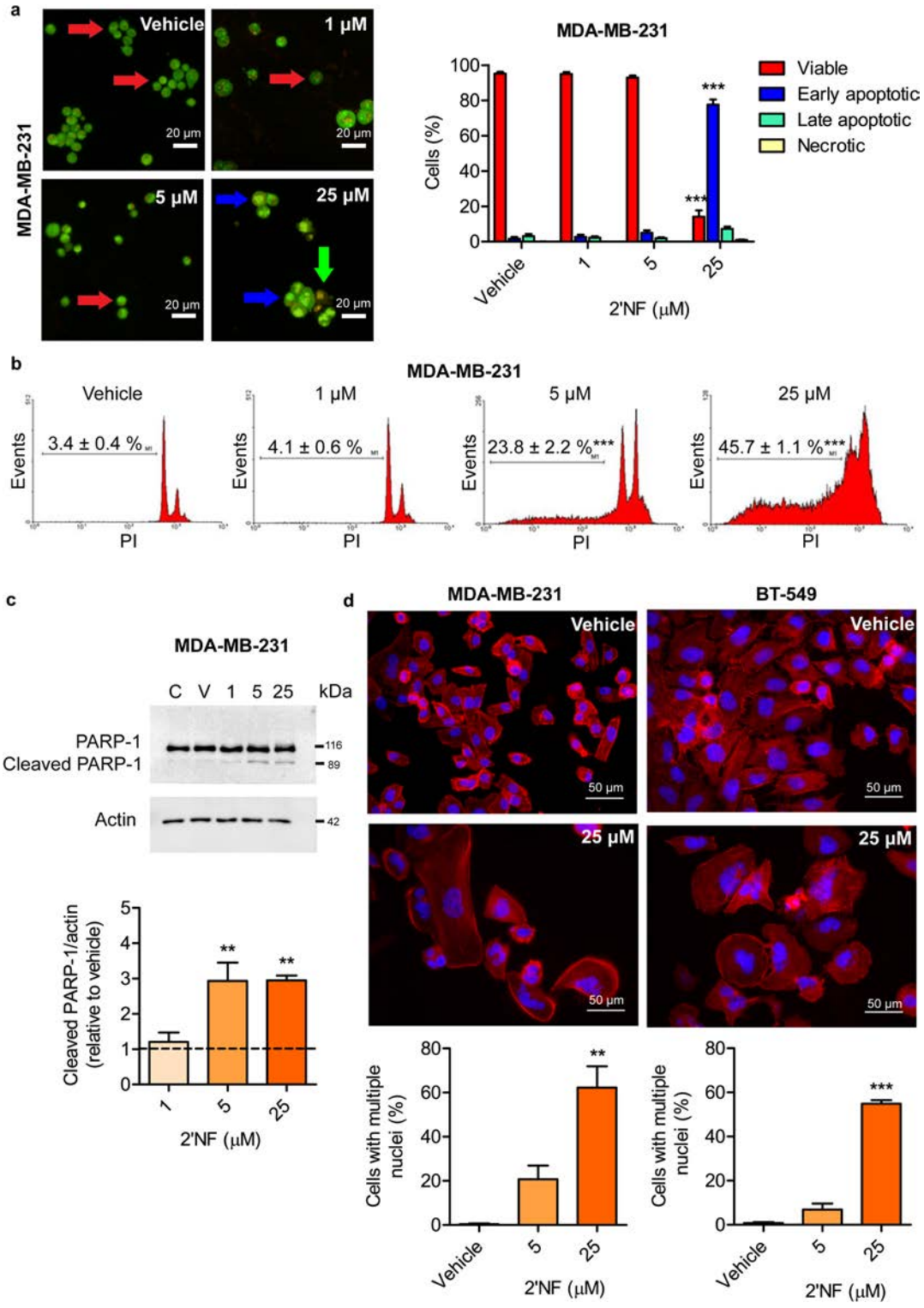

(TNKS), androgen receptor, aryl hydrocarbon receptor, or estrogen receptor α/β might be related to its antitumor effects. Among these targets, three proteins—PARP1, TNKS1 (PARP5a), and TNKS2 (PARP5b)—belong to the same family of PARPs. Some flavones have been shown to interact with PARP1[26] and TNKS1/2[27,28]. Regarding nitroflavones such as 2'NF, a synthetic nitroflavone derivative has been shown to interact with PARP1[29]; however, no publications to date have reported TNKS1/2 as ligands for nitroflavones. Therefore, we considered PARP1 as a suitable target for evaluating its potential interaction with 2'NF.

Computational docking studies were carried out using Molecular Operating Environment (MOE)™ tool to assess the interaction between 2'NF[30] (Fig. 1) and PARP1 (PDB ID 7KK4)[31]. Through this analysis, the 5 lowest energy poses were obtained and the interaction energy of the best achieved pose (Fig. 8a) rendered − 6.5262 kcal/mol. Protein ligand interaction fingerprint (PLIF) analysis revealed that 2'NF would interact with the catalytic domain of PARP1. In particular, hydrogen bond acceptor-type interactions were observed with the main chain

Fig. 3. 2'NF induces apoptosis and mitotic catastrophe in TNBC cells. (**a**) Dual acridine orange and ethidium bromide fluorescent staining was performed to evaluate MDA-MB-231 cell apoptosis after treatment with 2'NF (1, 5 and 25 μM) or vehicle for 72 h. Left panel: representative microphotographs. Cell coloring staining is observed as viable cell: green; early apoptotic cell: green with brilliant dots in the nuclei, associated to chromatin condensation and nuclear fragmentation; late apoptotic cell: orange, with chromatin condensation and nuclear fragmentation; necrotic cell: orange, without chromatin condensation. Red arrow: viable cell; blue arrow: early apoptotic cell; green arrow: late apoptotic cell. Scale bar: 20 μm. Right panel: cell percentages for each condition corresponding to mean ± SEM (n = 4–6 independent experiments); two-way ANOVA followed by Bonferroni´s post-test. ***$p < 0.001$, with respect to vehicle. (**b**) Percentages of hypodiploidy (sub-G_1 phase) were determined in MDA-MB-231 cells treated with 2'NF (1, 5 and 25 μM) or vehicle for 72 h. Cells were stained with propidium iodide (PI) to perform flow cytometry, which was evaluated using WinMDI software. Results correspond to mean ± SEM (n = 4–7 independent experiments); one-way ANOVA followed by Dunnett´s post-test. ***$p < 0.001$, respect to vehicle. (**c**) PARP1 cleavage as a parameter of apoptosis was analyzed by Western blotting. Cleaved PARP1 (89 kDa fragment) versus intact PARP1 was estimated in MDA-MD-231 cells treated with 2'NF (1, 5 and 25 μM) or vehicle for 72 h. Actin: loading control. Densitometric results correspond to mean ± SEM (n = 3 independent experiments); one-way ANOVA followed by Dunnett´s post-test. **$p < 0.01$, respect to vehicle (V, 1, dashed line). C: control (non-treated cells). Representative original blots are presented in Fig. S4. (**d**) MDA-MB-231 and BT-549 cells were treated with 2'NF for 72 h or vehicle. Upper panel: representative microphotographs of cells stained with TRITC-phalloidin to detect actin microfilaments (red) and counterstained with DAPI to identify nuclei (blue). Scale bar: 50 μm. Lower panel: Cells with multiple nuclei (> 2) were counted. Results correspond to mean ± SEM (n = 3 independent experiments); one-way ANOVA followed by Dunnett´s post-test. **$p < 0.01$; ***$p < 0.001$, respect to vehicle.

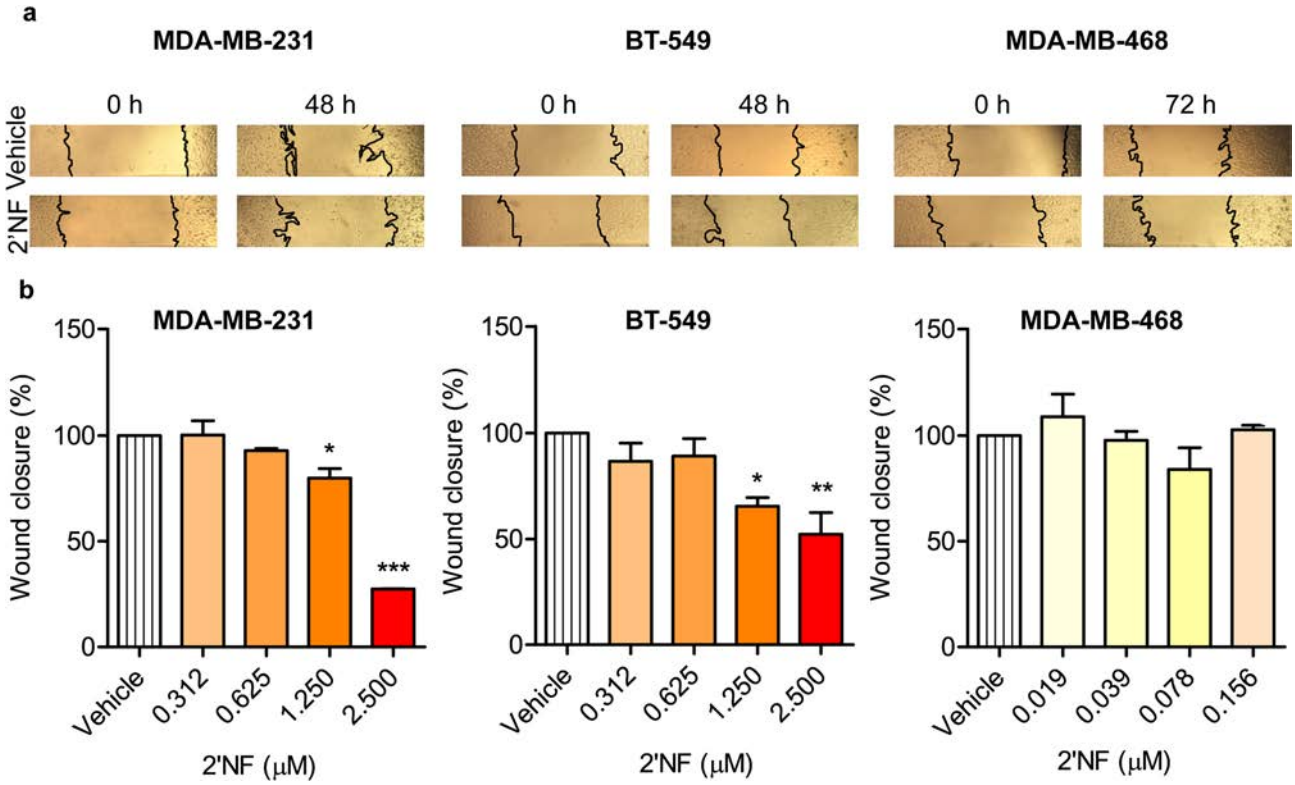

Fig. 4. The flavonoid 2'NF inhibits TNBC cell migration. MDA-MB-231, MDA-MB-468 and BT-549 cells were seeded onto 96-well plates and were allowed to grow to confluence in the presence of 10% FBS for 48 h at 37 °C. Then, a scratch was performed using a tip, and cells were washed and cultured with various concentrations of 2'NF or vehicle in the absence of FBS, during different times at 37 °C. Cells were photographed at initial (0 h) and final incubation time (48 or 72 h). (**a**) Representative microphotographs of wounds at the highest 2'NF concentration tested (2.500 μM for MDA-MB-231 and BT-549 cells, 0.156 μM for MDA-MB-468 cells) at 0 h, and 48 or 72 h. Magnification: ×40. (**b**) Image J software was used to determine the whole area of wounds in photographs, at initial (0 h) and the final incubation time (48 or 72 h), and wound closure was calculated as follows: wound closure (%) = [(area at 0 h—area at final time) / area at 0 h] × 100. Percentages of wound closure at the final incubation time versus 0 h correspond to mean ± SEM (n = 3–4 independent experiments); one-way ANOVA followed by Dunnett´s post-test. *$p < 0.05$; **$p < 0.01$; ***$p < 0.001$, respect to vehicle (100%).

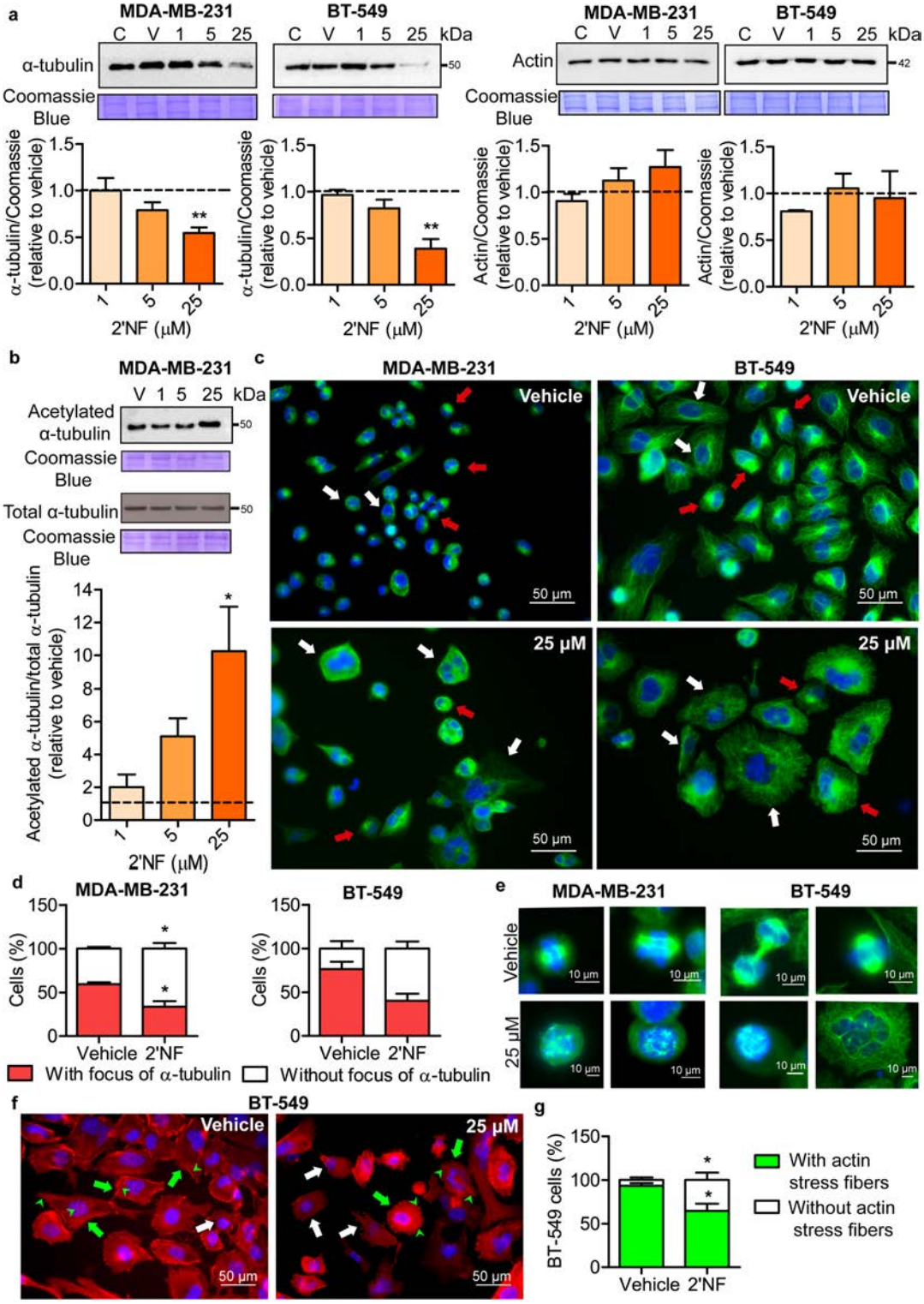

of Gly863 residue and with the side chain of Ser904, a hydrophobic interaction with Tyr896, and a hydrogen bond acceptor-type interaction with a water molecule (X-872) (Fig. 8a).

Next, molecular dynamics approach was performed to further study the interactions between 2'NF and PARP1. The lowest energy pose between the crystallographic structure of PARP1 (PDB ID 7KK4)[31] and 2'NF obtained in molecular docking studies (Fig. 8a) was used as a starting point. The apo form of PARP1 (without the ligand) was also simulated under identical conditions for comparative analysis. The system's total energy is presented in Fig. S3. The root-mean-square deviation (RMSD) over time indicated that both systems reached a stable equilibrium after approximately 20 ns. The PARP1–2'NF complex exhibited an average RMSD of 2.21 ± 0.21 Å, while the apo form showed a higher average RMSD of 2.75 ± 0.30 Å (Fig. S3). The shortest distance and lowest energy interactions found were hydrogen bonding between 2'NF and PARP1 Gly863, Tyr896 and Ser904 residues (Figs. 8b and c, S3). The preferred interaction types were hydrogen bonding, π–π interaction

◀**Fig. 5**. 2'NF alters α-tubulin and actin cytoskeleton on TNBC cells. (**a**) MDA-MB-231 and BT-549 cells were treated with 1, 5, and 25 μM of 2'NF for 72 h. Western blotting assays were used to detect α-tubulin and actin levels, after which membranes were stained with Coomassie brilliant blue as a loading control. C: control; V: vehicle. Results are presented as the mean ± SEM (n = 3–8 independent experiments); one-way ANOVA followed by Dunnett's post-test. $^{**}p < 0.01$ respect to vehicle (1, dotted line). (**b**) MDA-MB-231 cells were treated with 1, 5 and 25 μM of 2'NF for 72 h. Protein samples were run on two parallel gels to detect acetylated α-tubulin and total α-tubulin levels by Western blotting, respectively. Membranes were subsequently stained with Coomassie brilliant blue to serve as a loading control. For densitometric analysis, the level of acetylated α-tubulin was normalized to total α-tubulin and then compared to the vehicle (V). Results are presented as the mean ± SEM from two independent experiments (n = 2); one-way ANOVA followed by Bonferroni's post-test. $^{*}p < 0.05$, respect to vehicle (dotted line). Representative original blots are presented in Figs. S5 and S6. (**c**) MDA-MB-231 and BT-549 cells were treated with 25 μM 2'NF or vehicle for 72 h. Cells were then fixed, permeabilized, and incubated with a primary anti-α-tubulin antibody, which was detected using the corresponding Alexa Fluor 488-conjugated secondary antibody. DAPI counterstaining was performed to detect nuclei. n = 2 independent experiments. Representative images of cells observed under fluorescence microscopy are shown. α-tubulin: green; nuclei: blue; red arrows: cells with an α-tubulin focus; white arrows: cells without an α-tubulin focus. Scale bar: 50 μm. (**d**) Percentages of cells with or without an α-tubulin focus near the nucleus were determined from photographs obtained in (**c**), at least 100 cells/experiment were examined for each condition. Results are presented as the mean ± SEM (n = 2 independent experiments); one-way ANOVA followed by Bonferroni's post-test. $^{*}p < 0.05$, respect to vehicle for each condition. (**e**) MDA-MB-231 and BT-549 cells were treated with 25 μM 2'NF or vehicle for 72 h, then fixed, permeabilized, and incubated with a primary anti-α-tubulin antibody, which was detected using the corresponding Alexa Fluor 488-conjugated secondary antibody. DAPI counterstaining was performed to detect the nuclei. n = 2 independent experiments. Representative images of vehicle-treated cells at different stages of cell division, exhibiting the characteristic bipolar mitotic spindle structure. Cells treated with 2'NF, which display multipolar mitotic spindles are shown. α-tubulin: green; nuclei: blue. Scale bar: 10 μm. (**f**) BT-549 cells were treated with 25 μM 2'NF or vehicle for 72 h, then fixed, permeabilized, and incubated with TRITC-phalloidin to detect F-actin. DAPI counterstaining was performed to detect the nuclei. n = 3 independent experiments. Representative images of cells observed under fluorescence microscopy after treatment with 2'NF or vehicle are shown. F-actin: red; nuclei: blue; green arrows: cells with stress fibers; white arrows: cells without stress fibers; green arrowheads: stress fibers. Scale bar: 50 μm. (**g**) Percentages of cells with or without stress fibers were determined from photographs obtained in (f), and at least 100 cells/experiment were examined for each condition. Results are presented as the mean ± SEM (n = 3 independent experiments); one-way ANOVA followed by Bonferroni's post-test. $^{*}p < 0.05$, respect to vehicle (100%).

with Tyr907 and π-cation with Lys903 (Fig. 8c). The frequency of hydrogen bonds with the protein and with the solvent was also analyzed (Fig. S3). Additionally, to evaluate changes in residue flexibility upon ligand binding, a ΔRMSF was calculated as the difference between the RMSF values of the PARP1–2'NF complex and those of the apo form. Positive ΔRMSF values indicate increased residue mobility in the presence of the ligand, whereas negative values suggest a reduction in flexibility upon binding. Notably, residues Gly863, Tyr896, and Ser904 exhibited consistently negative ΔRMSF values, indicating that their interactions with 2'NF are particularly stable. These results suggest that the ligand-binding site is characterized by very low conformational flexibility (Fig. 8d). Besides, 2'NF interaction energy with PARP1 and solvent was calculated (Fig. S3). Finally, the estimated binding energy value (ΔG = − 18.7 ± 3.7 kcal/mol) suggests a thermodynamically favorable binding between 2'NF and PARP1. Thus, these findings indicate that 2'NF has the potential to bind to PARP1 (PDB ID 7KK4) forming a thermodynamically stable complex.

PARP activity is inhibited by 2'NF

The presence of poly(ADP-ribose) (PAR) polymer was assessed in TNBC cells as a product of PARP activity, using an anti-pan-ADP-ribose binding reagent by Western blotting. As expected, PAR polymer level almost completely decreased after 2 h-treatment of MDA-MB-231 cells with olaparib (200 nM), a pharmacological PARP inhibitor[32] (Fig. 8e). Interestingly, 2'NF (40 μM) showed a tendency to decrease PAR levels in MDA-MB-231 cells (0.72 ± 0.03 and 0.68 ± 0.09 after 6 and 24 h-treatment, respectively) and MDA-MB-468 cells (0.60 ± 0.14 after 4 h-incubation), with respect to vehicle (1) (Fig. 8e). These results suggest a potential inhibitory effect of 2'NF on PARP activity in human TNBC cells.

Discussion

In this work, we investigated the effects of the synthetic flavonoid 2'NF on TNBC progression. While previous studies demonstrated antineoplastic effects of 2'NF in various cancer cell lines[21–23,33–35], its impact on TNBC had not been explored. We first evaluated the effects of 2'NF on cell viability, proliferation, and survival in three human TNBC cell lines. MTT assays showed a reduction in cell viability, with IC_{50} values ranging from 4 to 9.2 μM after 72 h, consistent with previous results in other cancer cell lines[34]. Accordingly, trypan blue exclusion assays revealed that 2'NF inhibited proliferation, particularly at concentrations higher than the IC_{50}. Colony formation assays further demonstrated that 2'NF reduced survival at lower concentrations. This flavonoid also altered cell cycle progression, increasing the percentage of cells in the S and G2/M phases while decreasing the G0/G1 population, suggesting cell cycle arrest at G2/M. Similar results were observed in other cancer cell lines, such as the cervical adenocarcinoma HeLa and human leukemia HL-60[21,22].

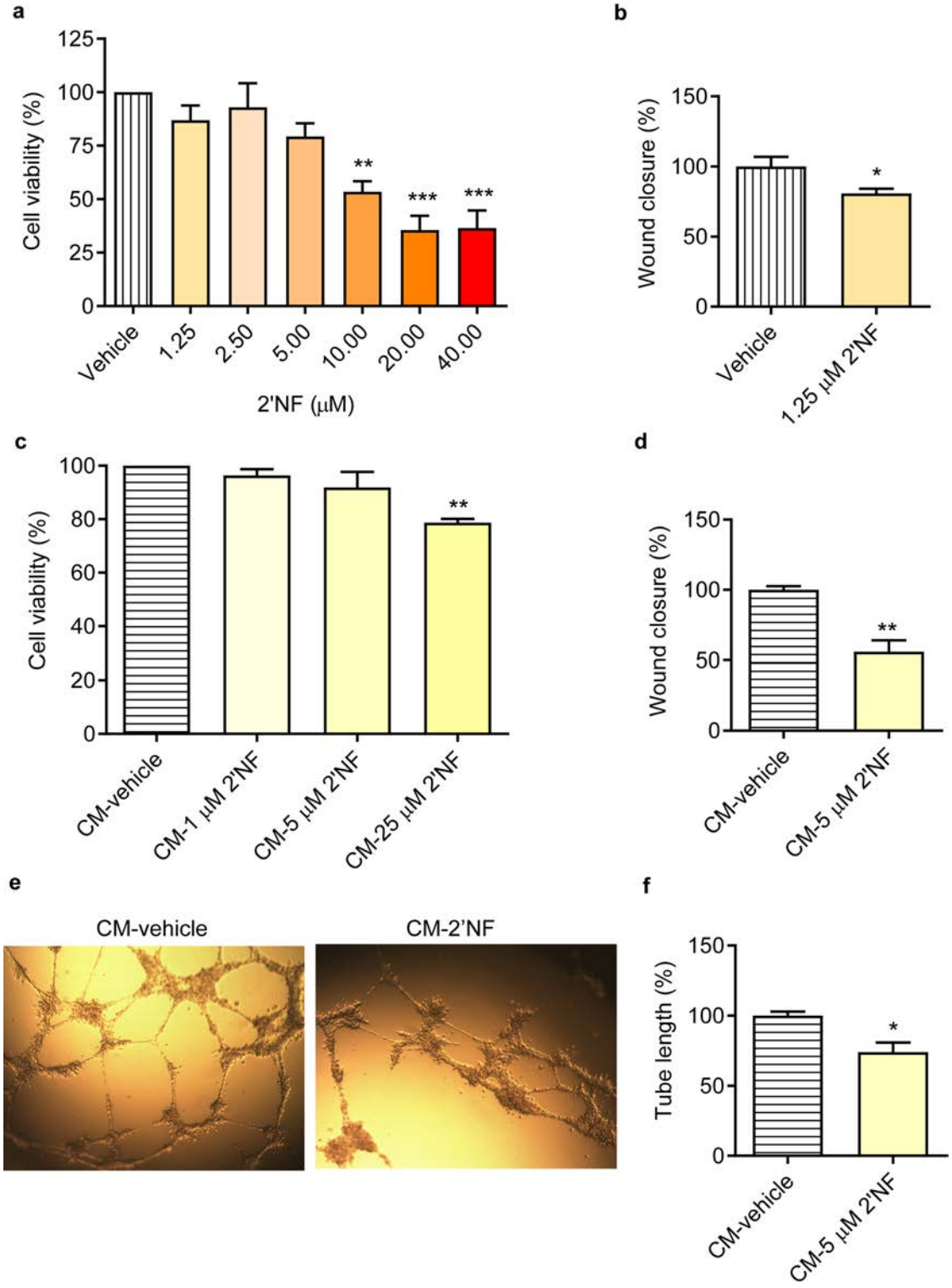

Furthermore, 2'NF induced apoptosis in MDA-MB-231 cells, evidenced by PARP1 cleavage and hypodiploidy, consistent with activation of caspases and apoptotic pathways as reported by others[36,37]. Previous studies have shown that 2'NF induces apoptosis through both death receptor and mitochondrial pathways in various cancer models[21,22] including the murine HER2$^+$ LM3 mammary cancer model[23]. Thus, our findings are in agreement with these results, as well as with studies on natural flavonoids in TNBC[17]. For instance, genistein, calcicopterin, and fisetin have shown similar effects in inhibiting proliferation, arresting the cell cycle, and inducing apoptosis in TNBC cell lines[18,20,38].

Interestingly, 2'NF also induced mitotic catastrophe, as evidenced by increased percentages of multinucleated MDA-MB-231 and BT-549 cells with enlarged cell size following treatment[39,40]. This process, a known oncosuppressive mechanism, may precede cell death or senescence[41–43]. Recently, this mechanism was also considered as a novel type of cell death accompanied by partial morphological and biochemical characteristics

◀**Fig. 6**. 2'NF reduces viability, migration and in vitro capillary-like tube formation of human endothelial cells. (**a**) EA.hy926 cells were treated with 2'NF or vehicle and cell viability was evaluated at 96 h using the MTT assay in the presence of 10% FBS. Results correspond to mean ± SEM (n = 3 independent experiments); one-way ANOVA followed by Dunnett´s post-test. $^{**}p < 0.01$; $^{***}p < 0.001$, respect to vehicle (100%). (**b**) Wound-healing assay in the presence of 1% FBS was evaluated at 24 h with 2'NF (1.25 µM) or vehicle. Percentages of wound closure at the final incubation time versus 0 h correspond to mean ± SEM (n = 4 independent experiments); unpaired Student's *t*-test. $^{*}p < 0.05$, respect to vehicle (100%). (**c**) Cell viability was evaluated at 24 h using the MTT assay in the presence of conditioned media (CM) derived from MDA-MB-231 cells pre-incubated with 2'NF (1, 5 and 25 µM) or vehicle (in the presence of 1% FBS for 72 h). Results correspond to mean ± SEM (n = 4 independent experiments); one-way ANOVA followed by Dunnett´s post-test. $^{**}p < 0.01$, respect to vehicle (100%). (**d**) Wound-healing assay in the absence of FBS was evaluated at 24 h in the presence of conditioned media (CM) derived from MDA-MB-231 cells pre-incubated with 2'NF (5 µM) or vehicle (in the presence of 1% FBS for 72 h). Percentages of wound closure at the final incubation time versus 0 h correspond to mean ± SEM (n = 3 independent experiments); unpaired Student's *t*-test. $^{**}p < 0.01$, respect to vehicle (100%). (**e**) Representative images of capillary-like tube formation of EA.hy926 cells cultured with CM derived from MDA-MB-231 cells pre-incubated with 2'NF (5 µM) or vehicle (in the presence of 1% FBS for 72 h). Magnification: ×40. n = 3 independent experiments. (**f**) Percentages of tube length (measured using Image J software) in EA.hy926 cells cultured with CM as in (**e**) correspond to mean ± SEM (n = 3 independent experiments); unpaired Student's *t*-test. $^{*}p < 0.05$, respect to vehicle (100%).

of apoptosis and necroptosis[44]. In turn, cell cycle arrest in G2/M is characteristic of this process[40,43]. Therefore, the observed G2/M arrest supports the hypothesis that 2'NF induces mitotic catastrophe, potentially triggering apoptosis as a subsequent event.

Additionally, the anti-migratory effects of 2'NF in MDA-MB-231 and BT-549 cells are a novel finding for this flavonoid. Several other flavonoids have demonstrated similar inhibition of MDA-MB-231 cell migration, including silybin, apigenin, luteolin, myricetin and baicalein[17]. The isoflavone formononetin also affected 4T1 TNBC cell migration[17]. On the contrary, 2'NF did not inhibit migration in MDA-MB-468 cells. This lack of effect may be due to their proliferation under the experimental conditions, which could have masked the influence of the flavonoid on migration. Moreover, MDA-MB-468 cells inherently exhibit low migratory capacity, which could further explain the observed results[45].

In relation to the α-tubulin cytoskeleton, 2'NF reduced α-tubulin protein levels, increased its acetylation, disrupted microtubule organization, and promoted the formation of multipolar mitotic spindles in human TNBC cells. Numerous antitumor drugs bind to tubulin and influence microtubule dynamics, either by inhibiting depolymerization or polymerization, acting as stabilizing or destabilizing agents, respectively[46]. Similar effects have also been observed with various flavonoids, which are associated with their antitumor activity[47,48].

Cells maintain a pool of α- and β-tubulin through a post-transcriptional regulatory mechanism known as tubulin autoregulation. This process involves soluble or unpolymerized tubulin recognizing and destabilizing its own mRNA[49,50]. In this context, increased levels of soluble tubulin, triggered by microtubule depolymerizing agents, lead to mRNA degradation and a subsequent reduction in α- and β-tubulin protein synthesis[51,52].

Some compounds reduce tubulin levels by inducing its degradation, which also disrupts microtubule polymerization. The natural compound withaferin A promoted proteasome-dependent degradation of α- and β-tubulin proteins, without affecting mRNA levels, in HeLa cervical adenocarcinoma and HCT116 colorectal carcinoma cell lines. This flavonoid also interacted with the colchicine-binding site on β-tubulin, and its covalent binding to the adjacent Cys239 residue was required for tubulin degradation. Furthermore, withaferin A inhibited microtubule polymerization in vitro[53].

Several small molecules induce proteasome-mediated degradation of α- and β-tubulin, often through covalent binding to the Cys239 residue on β-tubulin. One example is T007-1, which triggered proteasome-dependent degradation of α- and β-tubulin and increased mRNA levels. In HeLa and HCT116 cells, T007-1 also inhibited tubulin polymerization in vitro[54].

Our immunofluorescence studies revealed a significant reduction of α-tubulin near the nucleus in cells treated with 2'NF. This pattern suggests a decrease in the density of microtubules radiating from the centrosome, which may be associated with the reduced α-tubulin protein levels. Thus, as 2'NF diminishes α-tubulin protein levels and promotes nuclear MTOC center vanishing, we propose it could be considered as a microtubule-destabilizing agent[46]. Future studies should evaluate the potential impact of 2'NF on microtubule polymerization-depolymerization, proteasome-dependent degradation of α-tubulin protein, and/or the degradation of its mRNA (a post-transcriptional regulatory mechanism).

Additionally, the increase in acetylated α-tubulin might also be associated with the effect of 2'NF on microtubule organization. Portran et al. showed that acetylated tubulin assembles more slowly and depolymerizes more rapidly than its deacetylated form[55]. Structurally, acetylation of α-tubulin weakens the interactions between microtubule protofilaments[55,56]. Furthermore, studies using acetylated and deacetylated microtubules showed that acetylation reduces microtubule stiffness, making them more flexible and resistant to mechanical breakage[55,57]. Given this, the increase in α-tubulin acetylation might be a mechanism through which 2'NF alters microtubule structure and dynamics. Additional studies are needed to assess the direct functional consequences of increased acetylated α-tubulin levels on microtubules and their organization following 2'NF treatment.

Within the cytoskeleton, actin filaments assemble into complex structures through interactions with specific proteins[58]. Among these structures are stress fibers, which are typically contractile due to their association with myosin II and are often anchored at focal adhesions[58,59]. We demonstrated that 2'NF reduced the arrangement

2'NF physicochemical properties	
Molecular weight	267.24 g/mol (Mi, SA)
Number of atoms	20 (Mi, SA)
Number of hydrogen bond acceptors	5 (Mi)
Number of hydrogen bond donors	0 (Mi, SA)
Number of rotatable bonds	2 (Mi, SA)
TPSA	76.03 $Å^2$
Log P	3.65 (Mi), 2.37 (SA)*
Water solubility	Moderate (− 6 < log S < − 4) (SA)
Volume	223.33 $Å^3$ (Mi)
Molecular refractivity	76.74 (SA)
Pharmacokinetics	
GI absortion/BBB permeant	High/yes (ads, SA)
P-gp substrate/inhibitor	No (ads y SA)/No (adS)
CYP1A2, CYP2C19, CYP2C9, CYP3A4 inhibitor	Yes (ads, SA)
OATP1B1,OATP1B3 inhibitor	Yes (adS)
OATP2B1, MATE1, OCT2, BSEP inhibitor	No (adS)
Log Kp (skin permeation)	− 5.52 cm/s (SA)
Drug-likeness (SA)	
Lipinski	Yes; 0 violation
Ghose	Yes
Veber	Yes
Egan	Yes
Muegge	Yes
Medicinal chemistry (SA)	
PAINS	0 alert
Brenk	2 alerts: nitro group, oxygen–nitrogen single bond
Leadlikeness	Yes
Synthetic accessibility score	3.02 (1 = very easy to 10 = very difficult)

Table 1. Physicochemical properties, pharmacokinetics, drug-like properties and medicinal chemistry of 2'NF. *TPSA* topological polar surface area; *Log P* water:octanol partition coefficient; *P-gp* P-glycoprotein; *CYP* cytochrome P450; *OATP* organic anion transporter polypeptide; *MATE* multidrug and toxin extrusion transporter; *OCT* organic cation transporter; *BSEP* bile salt export pump; *Kp* skin permeability coefficient. *PAINS* pan-assay interference compounds. *Brenk* refers to structures that are putatively toxic, chemically reactive, metabolically unstable, or have poor pharmacokinetics[82]. *GI* gastrointestinal; *BBB* blood–brain barrier. Parameters were obtained using Molinspiration (Mi), SwissADME (SA) and/or admetSAR (adS) software, as indicated in parentheses. *LogP consensus: average of five predictions obtained with different models. Aqueous solubility: refers to the following log S scale generated by the SA software: less than − 10, insoluble; between − 10 and − 6, poorly soluble; between − 6 and − 4, moderately soluble; between − 4 and − 2, soluble; between − 2 and 0, very soluble; greater than 0, highly soluble. Number of hydrogen bridge acceptors: determined by Mi according to the number of oxygen and nitrogen atoms.

of stress fibers in BT-549 cells. However, this effect was not associated with a reduction in actin protein levels, as these levels remained constant, unlike what was observed for α-tubulin. Thus, the reduction in stress fibers caused by 2'NF could be due to inhibition of their assembly or induction of their disassembly. Similar to microtubules, actin filaments exhibit dynamic behavior. Indeed, several molecules that interfere with actin filament polymerization and depolymerization exhibit anticancer activity[60]. Considering this, 2'NF might reduce stress fibers by promoting the depolymerization or by inhibiting the polymerization of actin filaments.

The effects of 2'NF on the actin cytoskeleton could also be associated with the formation of multinucleated cells. The assembly of actin and myosin II, similar to that found in stress fibers, is necessary for the formation of the contractile ring during cytokinesis[61,62]. Additionally, molecules that disrupt actin filament dynamics, such as cytochalasin B, can inhibit cytokinesis[60]. Failure of cytokinesis during cell division is one mechanism leading to the formation of multinucleated cells and mitotic catastrophe[63,64]. Therefore, the potential effect of 2'NF in promoting depolymerization or inhibiting polymerization of actin filaments could lead to inhibition of cytokinesis, subsequent formation of multinucleated cells, and induction of mitotic catastrophe. Moreover, when cytokinesis fails, the resulting tetraploid cells also contain double number of centrosomes, which is one of the key factors in the formation of multipolar spindles[65].

The main causes of mitotic spindle multipolarity include centrosome amplification, often due to failed cytokinesis or centriole overduplication. Another cause is the loss of spindle pole integrity, which can result from

pericentriolar material fragmentation or centriole dissociation[65]. Additionally, spindle multipolarity caused by spindle pole integrity loss has been correlated with mitotic delay or arrest[65].

Therefore, one possible hypothesis is that the formation of multipolar spindles after 2'NF treatment is a consequence of increased centrosome number caused by cytokinesis failure in multinucleated cells. However, other mechanisms may also contribute to 2'NF-induced spindle multipolarity. For instance, low doses of clinically used microtubule-targeting drugs induced multipolar spindles in TNBC cells (Cal51 and MDA-MB-231) and in patient-derived metastatic breast tumor cells. At these doses, multipolar divisions caused chromosomal instability and led to cell death without inducing mitotic arrest[66]. Cells undergoing multipolar divisions usually die through mitotic catastrophe, a mechanism that prevents chromosomal instability[40,43]. Moreover, it is well known that microtubule-stabilizing and -destabilizing antitumor drugs induce mitotic catastrophe[44,67].

Mitotic catastrophe is triggered by mitotic alterations and is typically accompanied by mitotic arrest[40]. Thus, 2'NF's effects on the cytoskeleton and mitotic spindle, leading to abnormal mitosis, might be the mechanisms through which this flavonoid induces mitotic catastrophe. In turn, 2'NF-induced cell cycle arrest could be a consequence of mitotic abnormalities. It is also worth noting the critical role of the cytoskeleton in cell migration. Actin filaments play a fundamental role in generating the force required for cell migration, while microtubules promote cell polarity and directional migration[68,69]. Therefore, disruption of microtubules and actin filaments may represent a mechanism by which 2'NF inhibits migration in TNBC cells.

2'NF acting directly or indirectly through CM from treated MDA-MB-231 cells also reduced viability, migration and capillary-like tube formation of human EA.hy926 endothelial cells, suggesting putative anti-angiogenic effects. Some other flavonoids have anti-angiogenic actions on endothelial and TNBC cells[17,70]. For example, the synthetic flavonoid LYG-202 reduced the formation of tube-like structures of EA.hy 926 endothelial cells treated with hypoxia-induced CM from MDA-MB-231 cells. In transwell assays, LYG-202 reduced EA.hy 926 cell migration and invasion promoted by MDA-MB-231 cells under hypoxia. This treatment also diminished F-actin and cytoplasmic stress fibers in EA.hy 926 cells[71]. Moreover, in silico studies predicted that 2'NF could inhibit *HIF1A* expression. Consistent with our predictions, eupatorin has also anti-angiogenic activity in MCF-7 and MDA-MB-231 cells by downregulating *HIF1A* and *VEGFA* (vascular endothelial growth factor A) expression[19].

The fundamental processes affecting the in vivo pharmacokinetics of a compound include Absorption, Distribution, Metabolism, and Excretion (ADME). Studying these processes is essential in early drug development[72]. Computational tools for predicting ADME parameters are valuable alternatives to experimental methods[73,74]. Using SwissADME[75] and admetSAR[76], we evaluated the physicochemical properties, pharmacokinetics, and drug-like characteristics of 2'NF. Our predictions indicated that 2'NF would have high gastrointestinal absorption and might cross the blood–brain barrier, highlighting its potential suitability for further investigation in the context of brain metastases, which are more frequent and have a worse prognosis in TNBC than in other breast cancer subtypes[77]. The flavonoid would be neither a substrate nor an inhibitor of P-glycoprotein (P-gp), one of the members of the P-gp family of ABC (ATP-binding cassette) transporters responsible for the efflux of drugs from cells, so it could passively diffuse across biological membranes. In addition, 2'NF could be co-administered with a P-gp substrate drug without affecting the pharmacokinetics of that compound. Importantly, 2'NF would inhibit liver transporters OATP1B1 and 1B3, relevant for co-administration with drugs like docetaxel and paclitaxel[78,79]. It would not inhibit BSEP, minimizing the risk of liver damage, and would inhibit cytochromes P450 (CYP) enzymes, including CYP3A4, suggesting caution in co-administration with CYP substrates, such as docetaxel and paclitaxel[80].

2'NF exhibits favorable drug-like characteristics, adhering to Lipinski's Rule of Five[81], therefore suggesting that it could be administered orally. Moreover, predictions show that this flavonoid lacks PAINS (Pan-assay interference compounds) structures, supporting its potential as a drug candidate. However, its nitro group and nitrogen–oxygen bond could be putatively toxic, chemically reactive, metabolically unstable or with poor pharmacokinetics[82], which requires further evaluation. Thus, its structure could be optimized to increase selectivity and potency against a therapeutic target, decrease adverse effects, if any, and/or increase its chemical stability. Besides, the synthetic accessibility score of 3.02 indicates that 2'NF is relatively easy to synthesize, as we proved herein, further supporting its potential for improved drug development. In conclusion, 2'NF shows promise as a drug candidate with favorable ADME properties and medicinal chemistry, being able to progress to later stages in drug development.

The antitumor effects of various flavonoids on TNBC have been previously demonstrated in vivo using models derived from MDA-MB-231 and 4T1 cells[17]. For example, the administration of icariin at daily doses of 20 and 40 mg/kg for 2 weeks inhibited the growth of tumors derived from MDA-MB-231 and 4T1 cells inoculated into *nude* and Balb/c mice, respectively[83]. Regarding 2'NF, previous findings in the murine HER2$^+$ breast cancer model showed that treatment with this flavonoid (10 mg/kg), administered twice weekly for 3 weeks, reduced tumor volume by 70%[23]. In this work, in a TNBC model using immunocompetent mice inoculated with 4T1 cells, daily treatment (5 times per week) with 2'NF at a dose of 20 mg/kg for 2 weeks promoted its antitumor effect, with a significant reduction in relative tumor volume starting on day 2 of treatment and a maximum reduction of 57% observed on day 9. However, the effect of 2'NF on TNBC tumor growth was less pronounced than in the HER2$^+$ model[23], suggesting that TNBC may exhibit greater resistance to 2'NF treatment than HER2$^+$ breast cancer. These differences could also be attributed to other unknown mechanisms induced by 2'NF perhaps linked to HER2 signaling pathways.

Treatment with 2'NF did not alter the weight of vital organs such as the heart, kidneys, and liver nor did it affect body weight of mice inoculated with 4T1 cells. These results suggest that 2'NF treatment did not show evident toxicity under the evaluated conditions. In agreement with these findings, in the HER2$^+$ model, treatment with 2'NF at a dose of 40 mg/kg did not produce histopathological effects on various organs[23].

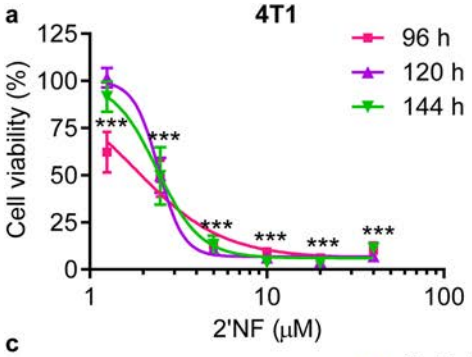

b

2'NF treatment (h)	IC_{50} (95% CI) (μM)
96	1.9 (1.5-2.5)
120	2.5 (2.3-2.7)
144	2.5 (2.1-2.9)

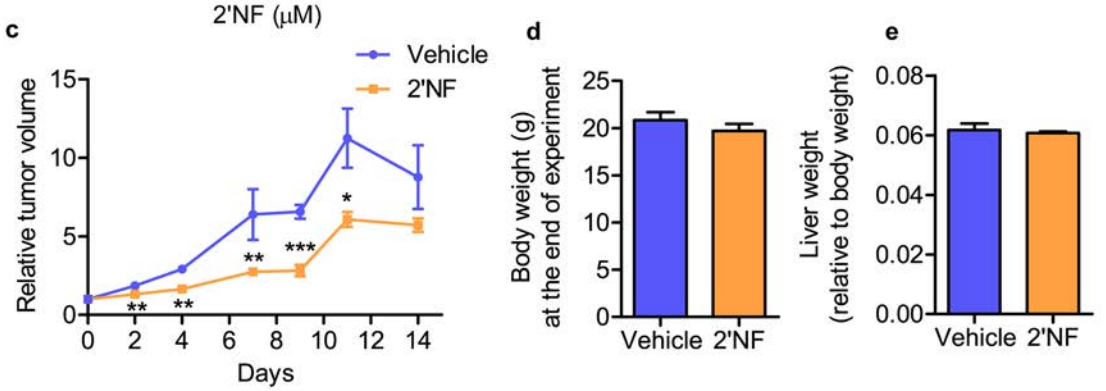

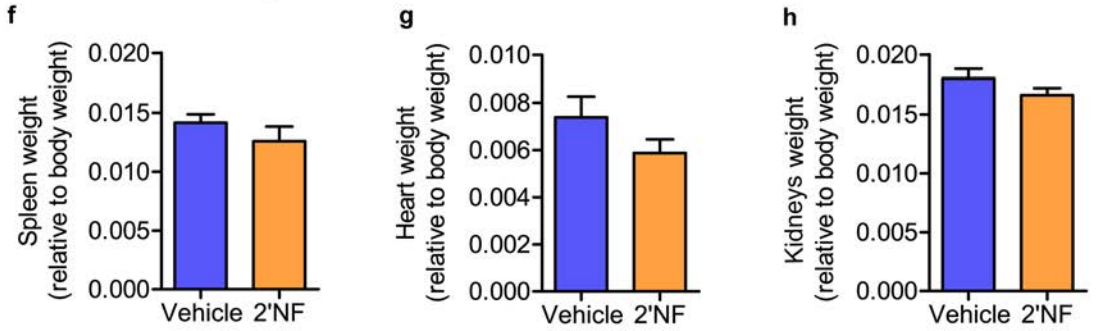

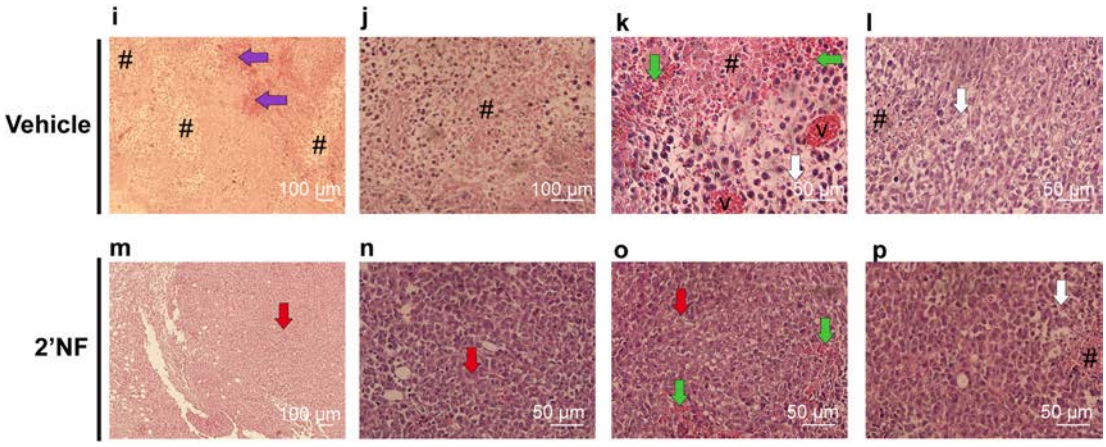

According to our in silico studies and previous reports, PARP1 could be a potential target for 2'NF. Molecular docking and molecular dynamics simulations showed that 2'NF interacts with the catalytic domain of PARP1, forming a thermodynamically stable complex. Consistently, 2'NF inhibited PARP activity in human TNBC cells.

PARP1 is protein composed of three primary domains: (1) an N-terminal DNA-binding domain, which includes three zinc-binding sites and a nuclear localization signal; (2) a central automodification domain, containing glutamate, aspartate and lysine residues, that serves as potential auto(ADP-ribosyl)ation acceptor, a leucine zipper that facilitates dimerization, and a BRCA1 C-terminal (BRCT) motif that binds phosphopeptides; and (3) a C-terminal catalytic domain, which features a tryptophan-, glycine- and arginine-rich (WGR) domain and the PARP signature sequence necessary for PAR synthesis[84]. PARP1 belongs to a family of enzymes that exhibit mono(ADP-ribosyl) and poly(ADP-ribosyl) transferase activity, and are responsible for repairing single-stranded DNA breaks before they progress to double-stranded breaks[85].

◀**Fig. 7**. 2'NF reduces TNBC tumor volume in vivo. (**a**) Viability of 4T1 cells was evaluated after treatment with 2'NF or vehicle using the MTT assay. Results correspond to mean ± SEM (n = 3–4 independent experiments). Significant differences respect to vehicle (100%) were determined using two-way ANOVA followed by Bonferroni´s post-test. ***$p < 0.001$. (**b**) 2'NF half-maximal inhibitory concentration (IC_{50}) values were obtained from dose–response viability curves after 96, 120 and 144 h-treatment using GraphPad Prism software. CI: confidence interval. (**c**) Approximately 1×10^5 syngeneic 4T1 cells were orthotopically inoculated in the abdominal mammary gland of female BALB/c mice. Once palpable tumors developed, 2'NF or vehicle was administered intraperitoneally (in 5–6 animals per group) at a daily dose (5 times per week) of 20 mg/kg for 2 weeks. The vehicle consisted of 10% DMSO, 60% PEG 400, and 30% saline (NaCl 0.9% in distilled water). During treatment, tumor measurements were recorded and relative tumor volume was calculated based on the volume recorded on the first day of treatment (day 0). Results are presented as mean ± SEM (of 3–6 animals per group). *$p < 0.05$, **$p < 0.01$, ***$p < 0.001$, compared to vehicle for each day (unpaired Student's *t*-test). (**d**–**h**) At the end of treatment, body weight and weights of liver, spleen, heart and kidneys (relative to the body weight) were recorded. Results are presented as mean ± SEM (of 3–4 animals per group) (unpaired Student's *t*-test). (**i**–**p**) At the end of treatment, tumors were excised, fixed, paraffin embedded and sliced to evaluate the histological characteristics on hematoxylin–eosin stained specimens. Representative microphotographs of histological sections of tumors treated with either 2′NF or vehicle after hematoxilin and eosin staining are shown. Vehicle panel: (**i**) Tumor Sect. (100×; scale bar: 100 µm) showing several extensive necrotic foci (#) and necro-hemorrhagic areas (purple arrows). (**j**) Tumor Sect. (200×; scale bar: 100 µm) displaying non-viable cells in necrotic regions (#). (**k**) Tumor Sect. (400×; scale bar: 50 µm) illustrating hemorrhagic foci (green arrows), necrosis (#), intense vasocongestion (v) and severe interstitial edema (white arrow). (**l**) Tumor Sect. (400×; scale bar: 50 µm) showing necrosis (#), cellular discohesion and interstitial edema (white arrow) in the parenchyma. 2′NF panel: (**m**) Tumor Sect. (100×; scale bar: 100 µm) revealing extensive areas of viable tumor cells with cellular cohesion (red arrow). (**n**) Tumor Sect. (400×; scale bar: 50 µm) showing viable tumor, cellular cohesion (red arrow) and reduced necro-hemorrhagic regions. (**o**) Tumor Sect. (400×; scale bar: 50 µm) evidencing preserved tumor parenchyma (red arrow) and minimal hemorrhage (green arrows). (**p**) Tumor Sect. (400×; scale bar: 50 µm) showing viable tumor cells with minimal necrosis (#) and a small area of cellular discohesion (white arrow).

2'NF target	Software
Poly [ADP-ribose] polymerase-1 (PARP1)	STP, TN, RF
Tankyrase-2 (TNKS2)	STP, SEA, RF
Tankyrase-1 (TNKS1)	
Androgen receptor	STP, TN, RF, adS
Cytochrome P450 1A2	TN, RF, adS
Cytochrome P450 2C9	
Amine oxidase [flavin-containing] A	TN, SEA, RF
Aryl hydrocarbon receptor	TN, SEA, RF
Hepatocyte nuclear factor 4-alpha	TN, SEA, RF
Estrogen receptor	TN, RF, adS

Table 2. 2'NF potential targets These targets were predicted simultaneously by at least three of the following software: SwissTargetPrediction (STP), TargetNet (TN), RandomForest QSAR (RF), SEA, SuperPred (SP) and admetSAR (adS).

PARP inhibitors (PARPi) have been developed to treat tumors with *breast cancer type 1 and type 2* gene (*BRCA1/2*) mutations, exploiting the concept of synthetic lethality (SL). SL occurs when the simultaneous loss of function of two different genes leads to cell death, while loss of only one gene is compatible with survival[86]. In cancer therapy, this strategy targets tumor cells carrying genetic mutations with drugs that inhibit another gene, thereby amplifying the defect. Based on this principle, the U.S. Food and Drug Administration (FDA) has approved PARPi such as olaparib and talazoparib for patients with metastatic TNBC harboring BRCA mutations[87].

Olaparib and talazoparib bind to the Tyr907 residue located at the catalytic domain of PARP1, and interact through hydrogen bonding with the nitrogen and carbonyl oxygen of the main chain of Gly863 and with the hydroxyl group of the side chain of Ser904[31]. Notably, hydrogen bond interactions with the nitrogen of Gly863 and the hydroxyl group of the Ser904 side chain were also found between 2'NF and PARP1 in our study. In fact, these interactions were among those with the lowest distance and energy. All current PARP1 inhibitors used in the clinic bind to the NAD^+-binding pocket of PARP1 and act as competitive inhibitors[88]. This binding leads to the trapping of PARP1 on DNA[87,88]. Thus, inhibition of PARP1 results in single-strand DNA breaks that cannot be repaired and are converted into double-strand breaks during replication. If homologous recombination repair (HRR) mechanisms are deficient, as occurs with mutations in *BRCA1/2*, double-strand breaks cannot be repaired, leading the cell towards apoptosis[89,90].

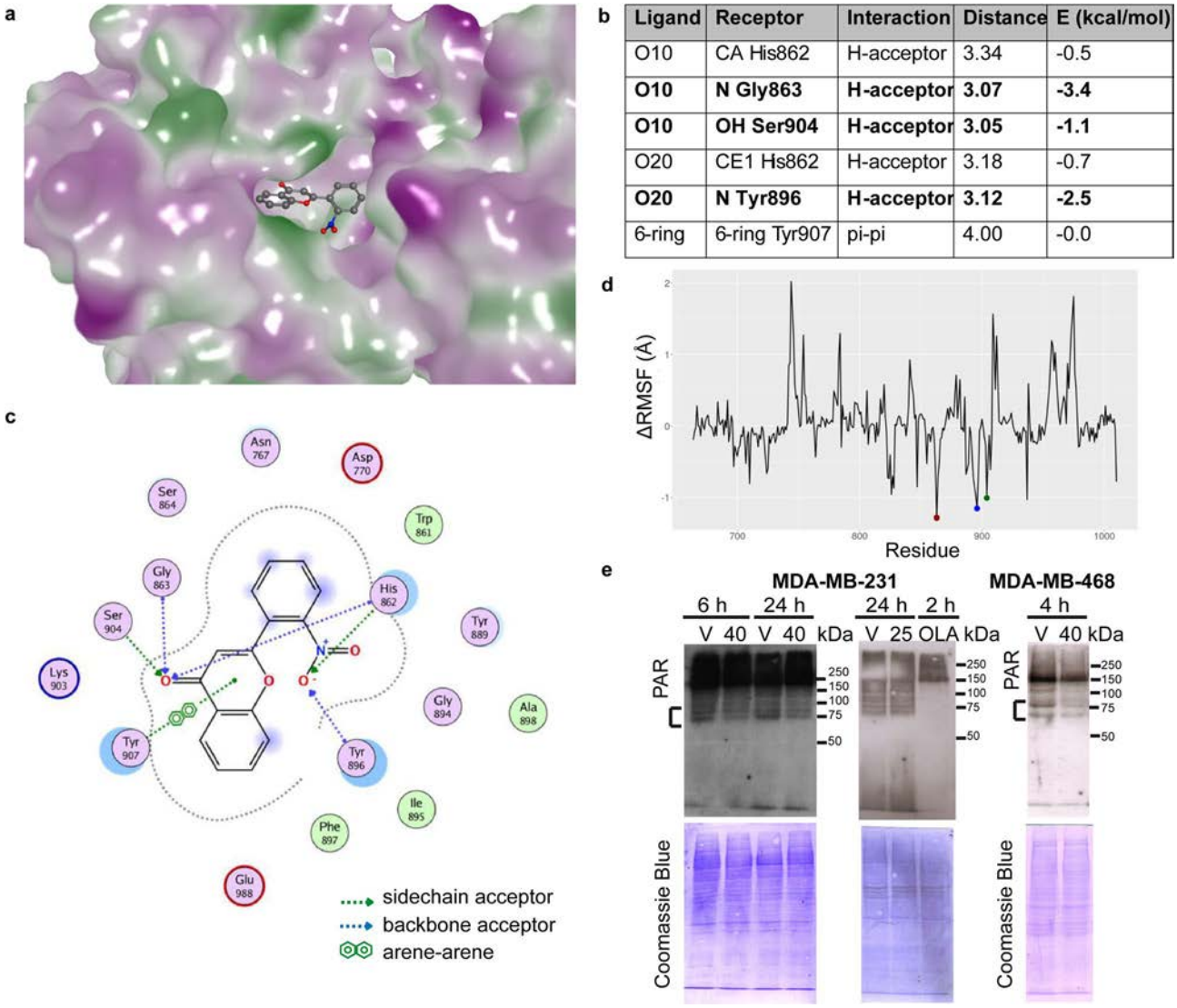

Ligand	Receptor	Interaction	Distance	E (kcal/mol)
O10	CA His862	H-acceptor	3.34	-0.5
O10	**N Gly863**	**H-acceptor**	**3.07**	**-3.4**
O10	**OH Ser904**	**H-acceptor**	**3.05**	**-1.1**
O20	CE1 Hs862	H-acceptor	3.18	-0.7
O20	**N Tyr896**	**H-acceptor**	**3.12**	**-2.5**
6-ring	6-ring Tyr907	pi-pi	4.00	-0.0

Fig. 8. 2'NF in silico interacts with the catalytic domain of PARP1. (**a**) Best Docking pose of 2'NF with PARP1 (PDB ID 7KK4). The protein surface is colored to represent lipophilic regions in green, hydrophilic regions in purple and neutral areas in white. 2'NF is shown in balls and sticks representation; grey: hydrocarbon chain, blue: nitrogen, red: oxygen. Molecular docking protocol validation is detailed in Additional Molecular docking information file and Fig. S8. (**b**) Main interactions between 2'NF and PARP1 obtained through Molecular dynamics. Interactions of lower distance and energy are highlighted in bold. CA: alpha carbon, N: nitrogen of the amino group, OH: hydroxyl group, CE: epsilon carbon. (**c**) Two dimensional plot of main interactions between 2'NF and PARP1 obtained through Molecular dynamics. Colored circles represent residues involved in the main interactions: pink: polar residues; green: nonpolar residues; pink with a red outline: acidic residues; and pink with a blue outline: for basic residues. Blue clouds represent solvent accessibility, and dotted line indicates the binding site. (**d**) ΔRoot-mean-square fluctuation (ΔRMSF), difference between the RMSF values of the PARP1–2'NF complex and those of the apo form, during Molecular dynamics. Red dot (Gly863), blue dot (Tyr896) and green dot (Ser904) all exhibited negative ΔRMSF values. (**e**) Effect of 2'NF on PARP activity in human TNBC cells. MDA-MB-231 and MDA-MB-468 cells were treated with 2'NF at 25 or 40 μM for 4, 6 and 24 h. As a control, cells were treated with olaparib (OLA, a pharmacological PARP inhibitor) at 200 nM for 2 h. Western blotting assays were used to detect the presence of poly(ADP-ribose) (PAR), although mono(ADP-ribose) could also be detected, and the membranes were subsequently stained with Coomassie brilliant blue as a loading control (n = 2 independent experiments). Molecular weights (kDa) are indicated to the right of each membrane. The two bands used for quantification of PAR levels are indicated with brackets. V: vehicle; 40: 2'NF at 40 μM; 25: 2'NF at 25 μM. Representative original blots are presented in Fig. S7.

However, most breast tumors are *BRCA*-proficient, with *BRCA* mutations occurring in only 10–20% of TNBC patients[91]. Therefore, efforts to overcome intrinsic or acquired resistance to PARPi have focused on combination therapies that exploit PARPi independently of *BRCA* status. One example is sacituzumab govitecan (IMMU-132), which combines the topoisomerase I inhibitor SN-38 with an anti–Trop-2 antibody, and has been clinically

tested in relapsed/refractory TNBC. Preclinical studies demonstrated that combining IMMU-132 with PARPi in TNBC models increased DNA damage compared to single-agent exposure, regardless of *BRCA1/2* status. This combination showed significantly enhanced antitumor effects in mice with both mutant and wild-type *BRCA* TNBC tumors[92]. In *BRCA*-proficient MDA-MB-231 xenografts, co-administration of guadecitabine, a DNA methyltransferase 1 (DNMT1) inhibitor, and talazoparib significantly reduced tumor volume, while PARPi alone had no effect[93]. Similarly, combining proto-oncogen *MYC* inhibition with PARPi induced SL in MYC-driven TNBC cells. *MYC* gene amplification correlates with RAD51 expression, a key enzyme in homologous recombination. Dinaciclib, a cyclin-dependent kinase inhibitor, downregulates MYC and, when combined with PARPi (niraparib), increases apoptosis, reduces proliferation, and raises sub-G1 cell cycle populations in both MDA-MB-231 and SUM149 (*BRCA*-mutant) cells. Importantly, MYC and RAD51 siRNAs, combined with PARPi, enhanced apoptosis and reduced clonogenicity and proliferation in these cells, indicating that MYC downregulation sensitizes TNBC to PARPi regardless of *BRCA* status[94].

Resistance to PARPi, including through *BRCA1/2* reversion, has been reported in breast cancer patients[95]. Remarkably, we found that 2'NF acts as a PARPi in *BRCA*-proficient TNBC cell lines (MDA-MB-231 and MDA-MB-468), which are generally more resistant than *BRCA*-mutant cells. In our work, PARP activity, catalyzing mono(ADP-ribose) and PAR polymer attachment, was evaluated in MDA-MB-231 (which lack mutations in HRR proteins) and MDA-MB-468 (which carry *PTEN* mutations) cells. PTEN (*phosphatase and tensin homolog deleted on chromosome ten*) loss destabilizes DNA replication forks by dissociating RAD51, impairing HRR, and making cells more sensitive to PARPi, similar to *BRCA1/2*-deficient cells[92]. Some other flavonoids have been shown to inhibit PARP1[96]; however, few studies have demonstrated their effects on PARP1 inhibition in cancer models. Docking experiments showed stable binding of amentoflavone (AMF), a natural flavonoid, to PARP1, with similar energy as that of olaparib. AMF also reduced PAR levels in vitro and enhanced anti-proliferative effects of carboplatin (a DNA-damaging chemotherapeutic) in A549 lung cancer cells, which was lost after *PARP1* knockdown. Oral AMF (100 mg/kg) combined with carboplatin significantly inhibited A549 tumor growth, decreased Ki67 expression, and increased apoptosis compared to carboplatin alone[26]. Additionally, the natural flavonoid luteolin directly binds PARP1 in surface plasmon resonance assays and exhibits strong inhibitory activity against the enzyme. Moreover, luteolin selectively induces the accumulation of DNA double-strand breaks and G2/M phase arrest in BRCA-deficient MDA-MB-436 TNBC cells[97]. Of note, beyond its role in DNA damage repair, PARP1 is also involved in other processes, such as mitosis[98]. Interestingly, PAR polymer is required for the assembly and function of the bipolar mitotic spindle[99], and some PARP1 inhibitors trigger mitotic catastrophe[44,100].

Our in silico studies also predicted the interaction of 2'NF with other PARP enzymes, such as TNKS1 and TNKS2. TNKS1/2 are PARP-domain-containing proteins that regulates WNT and NOTCH signaling, telomere maintenance, homologous recombination-mediated DNA damage response, Golgi trafficking, mitosis and apoptosis[101]. Remarkably, polymerization of PAR by TNKS1 was found to be required for spindle structure and function[102]. Thus, we cannot exclude the possibility that the effects of 2'NF on TNBC cells may also result from its interaction with TNKS1 or TNKS2. Since flavones and flavone-based compounds[27,28,103] have been reported as TNKS1/2 inhibitors (e.g., the flavone MN-64[104,105] and AZ-6102[106]), the potential promiscuity versus selectivity of 2'NF binding to PARP1, TNKS1, and TNKS2 should be carefully evaluated in future studies to avoid off-target effects within the PARP family. To address this, further in silico and crystallographic analyses, as well as cell-free assays such as surface plasmon resonance studies[107,108], would be valuable to determine the selectivity of 2'NF among different PARP family members.

Limitations of the study

Although this study provides robust in vitro and in vivo evidence supporting the antitumor activity of 2'NF, several limitations contextualize the conclusions. Computational analyses suggest a favorable pharmacological profile and no evident toxicity was observed in vivo; however, detailed pharmacokinetic, biodistribution, and long-term toxicity studies were not experimentally addressed and warrant further investigation. In addition, the in vivo experiments should be extended to other animal models, such as xenograft models generated by inoculating MDA-MB-231 cells into immunosuppressed mice, to evaluate the effects of 2'NF on tumor growth and angiogenesis in a human TNBC context. Moreover, the in vivo antitumor activity of 2'NF was assessed only as a single agent. Therefore, future studies exploring its efficacy in combination with standard chemotherapeutic agents and in comparison with approved PARP inhibitors will be important to determine its therapeutic relevance in clinically relevant settings.

With respect to the mechanism of action, the selectivity versus potential promiscuity of 2'NF binding across different members of the PARP family remains to be fully addressed. In silico analyses predicted interactions not only with PARP1 but also with other PARP enzymes, including TNKS1 and TNKS2. Furthermore, PARP activity was evaluated by Western blotting using a pan-ADP-ribose binding reagent, which detects enzymatic activity associated with both PARP1 and PARP3. Consequently, the specific PARP enzyme(s) inhibited by 2'NF cannot be conclusively identified in the present study. This issue should be carefully addressed in future work to better define target specificity and minimize potential off-target effects.

Finally, although our data indicate that 2'NF exhibits microtubule-targeting activity and anti-tubulin effects, the precise molecular mechanisms underlying these observations remain unclear. In particular, it is not yet known whether 2'NF promotes α-tubulin mRNA or protein degradation, or whether it acts as a microtubule-destabilizing agent by inhibiting polymerization or enhancing depolymerization. Additional mechanistic studies will be required to clarify these aspects.

Conclusion

In summary, 2'NF reduces the viability, survival, and proliferation of human TNBC cells. The mechanisms underlying these effects include G2/M phase cell cycle arrest and cell death via apoptosis and mitotic catastrophe. Additionally, 2'NF disrupts the cytoskeleton and inhibits the migration of human TNBC and endothelial cells, as well as in vitro angiogenesis. In vivo, using a TNBC model in immunocompetent mice, 2'NF delays tumor growth. Moreover, in silico analyses indicate that 2'NF forms a thermodynamically stable complex with the catalytic domain of PARP1, and cellular assays demonstrate inhibition of PARP enzymatic activity in *BRCA*-proficient TNBC cells. Taken together, our findings support the potential of 2'NF as a preclinical candidate for further investigation and as a scaffold for the development of compounds that could be explored in future combination strategies for TNBC. Further studies are warranted to elucidate additional mechanisms underlying the cytoskeletal and mitotic alterations induced by 2'NF.

Materials and methods

Antibodies

Anti-PARP1 (Cat #9542), HRP anti-mouse IgG (Cat #7076) and HRP anti-rabbit IgG antibodies (Cat #7074) were purchased from Cell Signaling Technology (Danvers, MA, USA). Anti-actin (Cat #A2066) and anti-acetylated α–tubulin (Cat #T7451) antibodies were obtained from Sigma-Aldrich (St. Louis, MO, USA). Anti-actin (Cat #PA5-78,715) and Alexa488 goat anti-mouse IgG (Cat #A-11029) antibodies were purchased from Invitrogen-Thermo Fisher Scientific (Waltham, MA, USA). Anti-α–tubulin (Cat #ab7291) antibody was purchased from Abcam (Cambridge, UK). An antibody-like reagent recognizing mono(ADP-ribose) and poly(ADP-ribose) (PAR) (Anti-pan-ADP-ribose binding reagent, Cat #MABE1016) from EMD Millipore Corporation (Burlington, MA, USA) was used to determine PARP activity.

Synthesis of 2′-nitroflavone (2'NF)

2'NF (IUPAC Name: 2-(2-nitrophenyl)chromen-4-one) (Fig. 1) was synthesized using Baker-Venkataraman transformation, as described previously[109,110]. This flavone was dissolved in dimethyl sulfoxide (DMSO, Sigma-Aldrich) as 100 mM stock solution and stored at − 20 °C. For in vitro assays, stock solution was diluted 1:10 (v/v) in ethanol and added at different concentrations to each culture medium. Vehicle was composed of DMSO: ethanol 1:9 (v/v), which was later diluted in the corresponding cell culture medium, as needed.

Cell culture

Human MDA-MB-231, MDA-MB-468, 4T1, and BT-549 TNBC cell lines were purchased from American Type Culture Collection (ATCC). MDA-MB-231 (ATCC HTB-26) and MDA-MB-468 (ATCC HTB-132) breast cancer cells were cultured in Dulbecco's modified Eagle's-F12 medium (Gibco-Invitrogen, Thermo Fisher Scientific), supplemented with 10% (v/v) heat-inactivated FBS (Natocor, Córdoba, Argentina), 2 mM L-glutamine, 100 µg/ml streptomycin and 100 units/ml penicillin. Murine 4T1 (ATCC CRL-2539) breast cancer cells were cultured in RPMI 1640 (Gibco-Invitrogen, Thermo Fisher Scientific), supplemented with 10% FBS, 2 mM L-glutamine, 100 µg/ml streptomycin and 100 units/ml penicillin. Human BT-549 (ATCC HTB-122) breast cancer cells were cultured in RPMI 1640, supplemented with 2.38 g/l Hepes, 0.11 g/l piruvate, 0.023 units/ml insulin, 10% FBS, 2 mM L-glutamine, 100 µg/ml streptomycin and 100 units/ml penicillin. EA.hy926 cells (ATCC CRL-2922) were maintained in DMEM (Gibco-Invitrogen, Thermo Fisher Scientific), supplemented with 10% FBS, 2 mM L-glutamine, 100 µg/ml streptomycin and 100 units/ml penicillin. All cell lines were cultured in a humidified 5% CO_2 incubator at 37 °C.

For some experiments, CM derived from MDA-MB-231 cells pre-incubated with 2'NF (1–25 µM) or vehicle for 72 h in the presence of 1% FBS were obtained.

Cell viability

Measurements of cell viability were determined using the 3-[4,5-dimethylthiazol-2-yl]-2,5-diphenyltetrazolium bromide (MTT, Sigma-Aldrich) assay. Briefly, MDA-MB-468, MDA-MB-231, BT-549, 4T1 and EA.hy926 cells were plated in 96-well plates in each culture medium plus 10% FBS, and allowed to attach for 24 h at 37 °C. Then, 1.25–40 µM 2'NF (final concentrations) or vehicle in each culture medium containing 10% FBS were added to the corresponding wells. In some experiments, other FBS concentrations were also tested. Afterwards, cells were incubated during different times at 37 °C. Finally, 10 µl of MTT solution (5 mg/ml) was added to each well, and the plates were incubated for an additional 4 h at 37 °C and centrifuged at 1500 × *g* for 10 min at room temperature. In order to solubilize the formazan crystals formed in viable cells, DMSO (200 µl) was added to each well before measuring the absorbance at 595 nm.

Trypan blue dye exclusion assay for cell proliferation

One volume of 0.4% trypan blue was mixed with one volume of cell suspension. Cells were counted within 3 to 5 min of mixing with trypan blue, as longer incubation periods will lead to cell death and reduced viability counts. A drop of the trypan blue/cell mixture was loaded onto a hemocytometer, and cells were counted. Unstained (viable) and stained (non-viable) cells were quantified separately, and the percentage of viable cells was calculated.

Colony formation

To evaluate the ability of single cells to form colonies, cells were loaded in 24-well plates in the corresponding culture medium with 10% FBS for 24 h at 37 °C. Then, treatment with 0.625–2.5 µM 2'NF or vehicle in culture medium plus 10% FBS was performed, incubating for 72 h. One change of media (2'NF or vehicle) was achieved

and cells were incubated at 37 °C. At day 7 (since cell loading), cells were washed, fixed in 4% paraformaldehyde and stained with 0.5% crystal violet in acetic acid 3% (v/v) for 20 min at room temperature. Colonies were photographed and quantified under a light microscope.

Flow cytometry analysis of cell cycle and DNA content

MDA-MB-231 (1×10^6) cells were incubated in culture medium with 10% FBS for 24 h at 37 °C, and then treated with 1 and 5 µM 2'NF (final concentrations) or vehicle for 72 h in the presence of 10% FBS. Single-cell suspensions were harvested, washed twice in phosphate-buffered saline (PBS), and fixed in 70% cold ethanol at 4 °C overnight. Finally, cells were washed and incubated with 50 µg/ml PI (Invitrogen Life Technologies, 300 µl) in 0.1% sodium citrate buffer, pH 8.4, containing 0.1% (v/v) Triton X-100 and 100 µg/ml RNAse A at 4 °C overnight. Cells were immediately analyzed in a FACscalibur flow cytometer (Becton Dickinson Biosciences, San José, CA, USA), and data were evaluated with Cylchred software. Evaluation of DNA content to study the proportion of hypodiploid cells was similarly performed in the presence of 1, 5 and 25 µM 2'NF or vehicle. Hypodiploid DNA content (sub-G1 phase) was analyzed in a FACscalibur flow cytometer and values were calculated using WinMDI 2.8 software.

Dual acridine orange (AO)/ethidium bromide (EB) fluorescent staining

MDA-MB-231 cells were incubated in 6-well-plates in culture medium with 10% FBS for 24 h at 37 °C, and then treated with 1, 5 and 25 µM 2'NF (final concentrations) or vehicle in the presence of 10% FBS for 72 h at 37 °C. Adherent cells from each well were harvested, but the culture medium from each well was also recovered in order to get apoptotic cells. After centrifugation, cells were treated with the staining solution containing 1:1 (v/v) 100 µg/ml AO and 100 µg/ml EB (AO/EB, Sigma-Aldrich). Cell morphology was immediately examined on coverslips, and quantified in at least 100 cells (3 different fields) within 20 min under a fluorescent microscope (Olympus BX50, Olympus, Japan).

Western blotting

Cells were harvested in lysis buffer (100 mM Tris, pH 7.4, 1% v/v Triton X-100, 10 mM EDTA, 2 mM PMSF and 0.012–0.034 units/ml aprotinin). Samples were resolved by SDS-PAGE under reducing conditions, as performed before[111]. Proteins were transferred to polyvinylidene-difluoride (PVDF) membranes (Bio-Rad Laboratories, Inc., Hercules, CA, USA) for immunoblotting with the indicated antibodies. After incubating with the corresponding horseradish-peroxidase (HRP)-conjugated secondary antibodies, immunoreactive bands were detected by chemiluminescence (ECL) with Pierce ECL Plus Western Blotting substrate (Thermo Fisher Scientific Inc., Waltham, MA, USA) in an ImageQuant™ LAS 500 (GE Healthcare Life Sciences, Illiniois, USA) detector. Densitometric analysis of protein levels was performed using ImageJ software (U.S. National Institutes of Health, Bethesda, MD, USA; http://rbsweb.nih.gov/ij/). More information is detailed in Additional Western blotting Information file.

Scratch wound assay

Cell migration was evaluated by means of the scratch wound assay. MDA-MB-231, MDA-MB-468, BT-549 and EA.hy926 cells were seeded onto 96-well plates and were allowed to grow to confluence in each culture medium in the presence of 10% FBS for 48 h at 37 °C. Then, a scratch was performed using a 20–200 µl tip, and cells were washed twice with each culture medium without FBS. Finally, 2'NF or vehicle were added and incubated in the absence of FBS (or in 1% FBS for endothelial cells) during different times at 37 °C. Final 2'NF concentrations were previously selected by MTT assay in the absence of FBS (or in 1% FBS for endothelial cells) to avoid affecting cell viability. Cells were photographed and Image J software was used to determine the whole area of the wound at the final incubation time versus 0 h (wound closure (%) = [(area at 0 h – area at final time) / area at 0 h] × 100).

Breast cancer model

All procedures involving animals were reviewed and approved by the Institutional Committee for the Care and Use of Laboratory Animals, Institute for Biomedical Research (BIOMED), School of Medical Sciences, Pontifical Catholic University of Argentina (UCA) (Ethical approval Nº: 001–2023). All animal protocols were supervised and managed by qualified trained personnel and were in accordance with recommendations from the National Institute of Health Guide for the Care and Use of Laboratory Animals (NIH Publications No. 8023) and ARRIVE guidelines (https://arriveguidelines.org).

Female BALB/c mice from School of Veterinary, National University of La Plata (Buenos Aires, Argentina) were bred and kept in ventilated cages at our animal health care facility at 22–24 °C, with food and water available ad libitum, 50–60% humidity and a 12 h-light/dark cycle. Animals with an age of 6–8 weeks and an average weight of 20–25 g were used. Breast tumors were generated in mice orthotopically inoculated in the abdominal mammary gland with 1×10^5 syngeneic 4T1 cells in 100 µl serum-free PBS, as described before[112]. Tumor volumes were determined by direct measurement with a caliper and calculated according to the following formula: $V = 4/3\ \pi \times [(\text{radius a} + \text{radius b})/2]^3$. When tumors were palpable, mice were randomly divided into two groups and daily treated with intraperitoneal injections of vehicle or 2'NF (20 mg/kg body weight; 100 µl)[23] dissolved in 10% DMSO, 60% polyethileneglycol (PEG) and 30% saline (0.9% NaCl) for 14 days. Afterwards, mice were then sacrificed by cervical dislocation, previously anaesthetized with ketamine (60–100 mg/kg) and xylazine (5–10 mg/kg) via intraperitoneal injection, and tumors and tissues were removed and weighed.

Histopathological studies

Tumors and tissues were excised, fixed in 4% (v/v) formaldehyde in PBS (formalin), paraffin embedded and sliced into 5-µm-thick sections to evaluate the histological characteristics on hematoxylin–eosin stained specimens, as previously described[113]. Dissemination was evaluated macroscopically ex vivo. A pathologist performed histological evaluation.

Immunofluorescence

To stain F-actin, MDA-MB-231 and BT-549 cells were grown on uncoated coverslips in 24-well plates in culture medium with 10% FBS for 24 h. Treatments were performed with 2'NF (5 and 25 µM) or vehicle in the corresponding culture medium with 10% FBS for 72 h at 37 °C. After washing with cold PBS, cells were fixed in 4% paraformaldehyde for 15 min, washed in PBS and permeabilized with PBS-0.5% (v/v) Triton X-100 for 10 min. After 3 washes in PBS-0.1% (v/v) Triton X-100, cells were incubated for 1 h in PBS-0.1% (v/v) Triton X-100 containing 1% (w/v) bovine serum albumin (BSA) to block nonspecific binding sites. Cells were treated with 5 µg/ml TRITC-phalloidin (Sigma-Aldrich) for 1 h, and then washed PBS-0.1% (v/v) Triton X-100. Cell nuclei were stained with 0.5 µg/ml 4',6-diamidino-2-phenylindole (DAPI). For α-tubulin fluorescent staining, permeabilized cells were incubated with the primary antibody overnight at 4 °C, followed by incubation with the green fluorescent Alexa-488-secondary antibody, and also counterstained with DAPI. Finally, coverslips were mounted with 1,4-diazabiciclo[2.2.2]octano (DABCO, Fluka, Steinheim, Germany) on glass slides, and cells were analyzed with an Olympus BX50 epifluorescence microscope (Olympus, Tokyo, Japan). Ten fields per coverslip were photographed.

In vitro capillary-like tube formation

Prechilled 96-well microtiter plates were coated with growth factor-reduced Geltrex (45 µl/well; Invitrogen Life Technologies) and incubated for 30 min at 37 °C. EA.hy926 cells (4×10^4) were loaded in each well in 50 µl DMEM without FBS. CM (50 µl) derived from TNBC cells (pre-incubated with 2'NF or vehicle for 72 h in the presence of 1% FBS) were added to each well. After 18 h, tube formation was analyzed under an inverted light microscope and 10 fields/well were recorded. Tubule lengths were measured using Image J software.

In silico drug-likeness, bioactivity and target predictions

Molinspiration (https://molinspiration.com) and SwissADME (ADME: Absorption, Distribution, Metabolism, and Excretion) (http://www.swissadme.ch)[75] software were used to evaluate 2'NF physicochemical properties. Pharmacokinetics, drug-likeness and medicinal chemistry friendliness of 2'NF were predicted using AdmetSAR (http://lmmd.ecust.edu.cn/admetsar2/)[76] and SwissADME software. Potential 2'NF bioactivities were estimated by Prediction of activity spectra for substances (PASS, http://www.ibmh.msk.su/PASS/)[114] software. Potential targets were predicted by SwissTargetPrediction (http://www.swisstargetprediction.ch)[115], TargetNet (http://targetnet.scbdd.com)[116], Random Forest QSAR (Quantitative structure–activity relationships; http://rfqsar.kaist.ac.kr)[117], SEA (Similarity ensemble approach; http://sea.bkslab.org)[118] and SuperPred (http://prediction.charite.de)[119] software.

Molecular docking and dynamics studies

Molecular docking studies were performed by using the crystal structure of 2'NF (at 100 K)[30] and the three-dimensional (3D) structure deposited at the Protein Data Bank (https://www.rcsb.org/pdb) of PARP1 catalytic domain (PDB ID: 7KK4) in complex with olaparib at 1.96 Å resolution[31]. We processed the crystallographic coordinates and ran our studies on MOE™ suite (Chemical Computing Group Inc. https://www.chemcomp.com)[120], including all crystallized water molecules, as we previously reported[121,122]. Through the Amber14-EHT force field, hydrogen atoms and charges were adjusted. The Triangle Matcher search algorithm was used to find the different 2'NF poses, and the London dG score function was used to estimate the affinity of each pose, from which the 30 most energetically favorable poses were selected. Then, the GBVI/WSA dG scoring function was used to select the 5 lowest energy poses. A protein ligand interaction fingerprint (PLIF) analysis was performed on the database containing these poses to obtain the relevant 2'NF interactions with PARP1 amino acids. Finally, the 3D structure of the best pose was analyzed and the binding energy of 2'NF with the protein was recorded. Protocol validation is detailed in Additional Molecular docking information file and Fig. S8.

Molecular dynamics simulation was performed from the crystallographic structure of PARP1 (PDB ID 7KKK4)[31] with the lowest energy pose obtained by molecular docking with 2'NF, as previously described[123]. The NAMD2 program package and a Charmm36 force field were used. For comparative purposes, we also simulated the apo form of PARP1 (in the absence of the ligand) under the same conditions. Molecular dynamics was performed at constant temperature and pressure (isobaric-isothermal ensemble, NPT). The whole procedure consisted of four stages under the following conditions: energy minimization: 20,000 steps (until a gradient of 0.1 kcal/mol/A^2 was reached), thermalization: from 0 to 310 K (37 °C) in 290 ps, equilibration: at 310 K for 1 ns (with restrained protein backbone), and production: at 310 K for 1 µs (with unrestrained protein backbone). Sampling for the evaluated properties was performed every 2 ps. During the simulation, the protein structural stability was analyzed by calculating the root-mean-square deviation (RMSD). In addition, the average mobility of the side chain of each residue was analyzed by calculating the root-mean-square fluctuation (RMSF). To assess changes in residue flexibility upon ligand binding, a ΔRMSF was computed as the difference between the RMSF values of the PARP1–2'NF complex and those of the apo form. Positive ΔRMSF values indicate residues that exhibit increased mobility in the complex compared to the apo form, whereas negative values reflect decreased mobility upon ligand binding. The interactions between 2'NF and PARP1 were also analyzed in terms of the type of interaction, the residues and atoms involved, the distance, the energy and the frequency. Finally, the binding free energy between 2'NF and PARP1 was estimated using the Molecular Mechanics/Poisson–Boltzmann

Surface Area (MM/PBSA) method[124]. The calculation was performed over 1000 frames extracted from the last 10 ns of the molecular dynamics simulation. The final binding free energy value corresponds to the average and standard deviation computed across these frames.

Statistical analysis

Data were analyzed using GraphPad Prism 8.0.2 software (GraphPad Software Inc., La Jolla, CA, USA) and results are expressed as the mean ± standard error of the mean (SEM). Differences between groups were assessed by one-way or two-way ANOVA (with appropriate post-tests) or by unpaired Student's *t*-test. Values of $p < 0.05$ were considered statistically significant.

Data availability

All the data generated or analyzed during this study are included in this published article and its supplementary information.

Received: 21 March 2025; Accepted: 26 December 2025
Published online: 03 January 2026

References

1. Perou, C. M. et al. Molecular portraits of human breast tumours. *Nature* **406**, 747–752 (2000).
2. Prat, A. et al. Phenotypic and molecular characterization of the claudin-low intrinsic subtype of breast cancer. *Breast Cancer Res.* **12**, R68 (2010).
3. Cancer Genome Atlas Network. Comprehensive molecular portraits of human breast tumours. *Nature* **490**, 61–70 (2012).
4. GLOBOCAN 2022. https://gco.iarc.who.int/today/en.
5. Lehmann, B. D. et al. Identification of human triple-negative breast cancer subtypes and preclinical models for selection of targeted therapies. *J. Clin. Invest.* **121**, 2750–2767 (2011).
6. Lehmann, B. D. et al. Refinement of triple-negative breast cancer molecular subtypes: Implications for neoadjuvant chemotherapy selection. *PLoS ONE* **11**, e0157368. https://doi.org/10.1371/journal.pone.0157368 (2016).
7. Lehmann, B. D. et al. Multi-omics analysis identifies therapeutic vulnerabilities in triple-negative breast cancer subtypes. *Nat. Commun.* **12**, 6276. https://doi.org/10.1038/s41467-021-26502-6 (2021).
8. Farghadani, R. & Naidu, R. The anticancer mechanism of action of selected polyphenols in triple-negative breast cancer (TNBC). *Biomed. Pharmacother.* **165**, 115170 (2023).
9. Sun, H. et al. Anti-angiogenic treatment promotes triple-negative breast cancer invasion via vasculogenic mimicry. *Cancer Biol. Ther.* **18**, 205–213 (2017).
10. Serrano García, L. et al. Patterns of immune evasion in triple-negative breast cancer and new potential therapeutic targets: A review. *Front. Immunol.* **15**, 1513421. https://doi.org/10.3389/fimmu.2024.1513421 (2024).
11. Ke, D. Y. J., El-Sahli, S. & Wang, L. The potential of natural products in the treatment of triple-negative breast cancer. *Curr. Cancer Drug Targets* **22**, 388–403 (2022).
12. Kumar, S. & Pandey, A. K. Chemistry and biological activities of flavonoids: An overview. *Sci. World J.* **2013**, 162750 (2013).
13. Ye, Q. et al. Reversal of multidrug resistance in cancer by multi-functional flavonoids. *Front. Oncol.* **9**, 487. https://doi.org/10.3389/fonc.2019.00487 (2019).
14. Heim, K. E., Tagliaferro, A. R. & Bobilya, D. J. Flavonoid antioxidants: Chemistry, metabolism and structure-activity relationships. *J. Nutr. Biochem.* **13**, 572–584 (2002).
15. Romano, B. et al. Novel insights into the pharmacology of flavonoids. *Phytother. Res.* **27**, 1588–1596 (2013).
16. Ullah, A. et al. Important flavonoids and their role as a therapeutic agent. *Molecules* https://doi.org/10.3390/molecules25225243 (2020).
17. Vachetta, V. S., Marder, M., Troncoso, M. F. & Elola, M. T. Opportunities, obstacles and current challenges of flavonoids for luminal and triple-negative breast cancer therapy. *Eur. J. Med. Chem. Reports* **6**, 100077 (2022).
18. Pan, H. et al. Genistein inhibits MDA-MB-231 triple-negative breast cancer cell growth by inhibiting NF-κB activity via the Notch-1 pathway. *Int. J. Mol. Med.* **30**, 337–343 (2012).
19. Razak, N. A. et al. Cytotoxicity of eupatorin in MCF-7 and MDA-MB-231 human breast cancer cells via cell cycle arrest, anti-angiogenesis and induction of apoptosis. *Sci. Rep.* **9**, 1514. https://doi.org/10.1038/s41598-018-37796-w (2019).
20. Moradi, M. et al. Flavonoid calycopterin triggers apoptosis in triple-negative and ER-positive human breast cancer cells through activating different patterns of gene expression. *Naunyn. Schmiedebergs. Arch. Pharmacol.* **393**, 2145–2156 (2020).
21. Cárdenas, M. G., Blank, V. C., Marder, M. & Roguin, L. P. 2'-Nitroflavone induces cell cycle arrest and apoptosis in HeLa human cervical carcinoma cells. *Cancer Lett.* **268**, 146–157 (2008).
22. Cárdenas, M. G., Blank, V. C., Marder, M. N. & Roguin, L. P. 2'-Nitroflavone induces apoptosis and modulates mitogen-activated protein kinase pathways in human leukaemia cells. *Anticancer. Drugs* **23**, 815–826 (2012).
23. Cárdenas, M. G., Zotta, E., Marder, M. & Roguin, L. P. In vitro induction of apoptosis and in vivo effects of a flavone nitroderivative in murine mammary adenocarcinoma cells. *Int. J. Cancer* **125**, 222–228 (2009).
24. Kunda, P. & Baum, B. The actin cytoskeleton in spindle assembly and positioning. *Trends Cell Biol.* **19**, 174–179 (2009).
25. McIntosh, J. R. Mitosis. *Cold Spring Harb. Perspect. Biol.* **8**, a023218 (2016).
26. Hu, X. L. et al. Identification of amentoflavone as a potent highly selective PARP-1 inhibitor and its potentiation on carboplatin in human non-small cell lung cancer. *Phytomedicine* **50**, 88–98 (2018).
27. Narwal, M., Haikarainen, T., Fallarero, A., Vuorela, P. M. & Lehtiö, L. Screening and structural analysis of flavones inhibiting tankyrases. *J. Med. Chem.* **56**, 3507–3517 (2013).
28. Alam, S. & Khan, F. 3D-QSAR, docking, ADME/Tox studies on flavone analogs reveal anticancer activity through Tankyrase inhibition. *Sci. Rep.* **9**, 5414 (2019).
29. Mitra, A., Biswas, R., Bagchi, A. & Ghosh, R. Insight into the binding of a synthetic nitro-flavone derivative with human poly (ADP-ribose) polymerase 1. *Int. J. Biol. Macromol.* **141**, 444–459 (2019).
30. Oskolkov, E., Kornilova, T., Chavez, P. A., Tillotson, J. P. & Timofeeva, T. V. Structural (at 100K) and DFT studies of 2'-nitro-flavone. *Acta Crystallogr. Sect. E Crystallogr. Commun.* **76**, 1417–1420 (2020).
31. Ryan, K. et al. Dissecting the molecular determinants of clinical PARP1 inhibitor selectivity for tankyrase1. *J. Biol. Chem.* **296**, 1–13 (2021).
32. Bochum, S., Berger, S. & Martens, U. M. Olaparib. In: *Small Molecules in Oncology. Recent results in cancer research.* (ed. Martens, U. M.) 217–233 (Springer, Cham, 2018).
33. Blank, V. C., Poli, C., Marder, M. & Roguin, L. P. Antiproliferative activity of various flavonoids and related compounds: Additive effect of interferon-alpha2b. *Bioorg. Med. Chem. Lett.* **14**, 133–136 (2004).

34. Cárdenas, M., Marder, M., Blank, V. C. & Roguin, L. P. Antitumor activity of some natural flavonoids and synthetic derivatives on various human and murine cancer cell lines. *Bioorganic Med. Chem.* **14**, 2966–2971 (2006).
35. Anselmi Relats, J. M. et al. Synergistic effect of the sphingosine kinase inhibitor safingol in combination with 2'-nitroflavone in breast cancer. *J. Mol. Med. (Berl)* **102**, 1503–1516 (2024).
36. Elmore, S. Apoptosis: A review of programmed cell death. *Toxicol. Pathol.* **35**, 495–516 (2007).
37. Pistritto, G., Trisciuoglio, D., Ceci, C., Garufi, A. & D'Orazi, G. Apoptosis as anticancer mechanism: Function and dysfunction of its modulators and targeted therapeutic strategies. *Aging (Albany NY)* **8**, 603–619 (2016).
38. Smith, M. L., Murphy, K., Doucette, C. D., Greenshields, A. L. & Hoskin, D. W. The dietary flavonoid fisetin causes cell cycle arrest, caspase-dependent apoptosis, and enhanced cytotoxicity of chemotherapeutic drugs in triple-negative breast cancer cells. *J. Cell. Biochem.* **117**, 1913–1925 (2016).
39. Vakifahmetoglu, H., Olsson, M. & Zhivotovsky, B. Death through a tragedy: Mitotic catastrophe. *Cell Death Differ.* **15**, 1153–1162 (2008).
40. Vitale, I., Galluzzi, L., Castedo, M. & Kroemer, G. Mitotic catastrophe: A mechanism for avoiding genomic instability. *Nat. Rev. Mol. Cell Biol.* **12**, 385–392 (2011).
41. Galluzzi, L. et al. Molecular definitions of cell death subroutines: Recommendations of the nomenclature committee on cell death 2012. *Cell Death Differ.* **19**, 107–120 (2012).
42. Galluzzi, L. et al. Molecular mechanisms of cell death: Recommendations of the nomenclature committee on cell death 2018. *Cell Death Differ.* **25**, 486–541 (2018).
43. Sazonova, E. V., Petrichuk, S. V., Kopeina, G. S. & Zhivotovsky, B. A link between mitotic defects and mitotic catastrophe: Detection and cell fate. *Biol. Direct* **16**, 25 (2021).
44. Bai, Z., Zhou, Y., Peng, Y., Ye, X. & Ma, L. Perspectives and mechanisms for targeting mitotic catastrophe in cancer treatment. *Biochim. Biophys. acta. Rev. cancer* **1878**, 188965 (2023).
45. Pfister, N. T. et al. Mutant p53 cooperates with the SWI/SNF chromatin remodeling complex to regulate VEGFR2 in breast cancer cells. *Genes Dev.* **29**, 1298–1315 (2015).
46. Naaz, F., Haider, M. R., Shafi, S. & Yar, M. S. Anti-tubulin agents of natural origin: Targeting taxol, vinca, and colchicine binding domains. *Eur. J. Med. Chem.* **171**, 310–331 (2019).
47. Mukhtar, E., Adhami, V. M., Sechi, M. & Mukhtar, H. Dietary flavonoid fisetin binds to β-tubulin and disrupts microtubule dynamics in prostate cancer cells. *Cancer Lett.* **367**, 173–183 (2015).
48. Liu, W., He, M., Li, Y., Peng, Z. & Wang, G. A review on synthetic chalcone derivatives as tubulin polymerisation inhibitors. *J. Enzyme Inhib. Med. Chem.* **37**, 9–38 (2022).
49. Gasic, I. & Mitchison, T. J. Autoregulation and repair in microtubule homeostasis. *Curr. Opin. Cell Biol.* **56**, 80–87 (2019).
50. Ohi, R., Strothman, C. & Zanic, M. Impact of the 'tubulin economy' on the formation and function of the microtubule cytoskeleton. *Curr. Opin. Cell Biol.* **68**, 81–89 (2021).
51. Ben-Ze'ev, A., Farmer, S. R. & Penman, S. Mechanisms of regulating tubulin synthesis in cultured mammalian cells. *Cell* **17**, 319–325 (1979).
52. Cleveland, D. W., Lopata, M. A., Sherline, P. & Kirschner, M. W. Unpolymerized tubulin modulates the level of tubulin mRNAs. *Cell* **25**, 537–546 (1981).
53. Yang, J. et al. The natural compound with Aferin A covalently binds to Cys239 of β-tubulin to promote tubulin degradation. *Mol. Pharmacol.* **96**, 711–719 (2019).
54. Yang, J. et al. Covalent modification of Cys-239 in β-tubulin by small molecules as a strategy to promote tubulin heterodimer degradation. *J. Biol. Chem.* **294**, 8161–8170 (2019).
55. Portran, D., Schaedel, L., Xu, Z., Théry, M. & Nachury, M. V. Tubulin acetylation protects long-lived microtubules against mechanical ageing. *Nat. Cell Biol.* **19**, 391–398 (2017).
56. Eshun-Wilson, L. et al. Effects of α-tubulin acetylation on microtubule structure and stability. *Proc. Natl. Acad. Sci. U. S. A.* **116**, 10366–10371 (2019).
57. Xu, Z. et al. Microtubules acquire resistance from mechanical breakage through intralumenal acetylation. *Science* **356**, 328–332 (2017).
58. Blanchoin, L., Boujemaa-Paterski, R., Sykes, C. & Plastino, J. Actin dynamics, architecture, and mechanics in cell motility. *Physiol. Rev.* **94**, 235–263 (2014).
59. Tojkander, S., Gateva, G. & Lappalainen, P. Actin stress fibers–assembly, dynamics and biological roles. *J. Cell Sci.* **125**, 1855–1864 (2012).
60. Trendowski, M. Exploiting the cytoskeletal filaments of neoplastic cells to potentiate a novel therapeutic approach. *Biochim. Biophys. Acta* **1846**, 599–616 (2014).
61. Robinson, D. N. & Spudich, J. A. Towards a molecular understanding of cytokinesis. *Trends Cell Biol.* **10**, 228–237 (2000).
62. Murthy, K. & Wadsworth, P. Myosin-II-dependent localization and dynamics of F-actin during cytokinesis. *Curr. Biol.* **15**, 724–731 (2005).
63. Ariizumi, T. et al. Multinucleation followed by an acytokinetic cell division in myxofibrosarcoma with giant cell proliferation. *J. Exp. Clin. cancer Res.* **28**, 44 (2009).
64. Mc Gee, M. M. Targeting the mitotic catastrophe signaling pathway in cancer. *Mediat. Inflamm.* **2015**, 146282 (2015).
65. Maiato, H. & Logarinho, E. Mitotic spindle multipolarity without centrosome amplification. *Nat. Cell Biol.* **16**, 386–394 (2014).
66. Zhou, A. S. et al. Diverse microtubule-targeted anticancer agents kill cells by inducing chromosome missegregation on multipolar spindles. *PLoS Biol.* **21**, e3002339. https://doi.org/10.1371/journal.pbio.3002339 (2023).
67. Nakayama, Y. & Inoue, T. Antiproliferative fate of the tetraploid formed after mitotic slippage and its promotion; a novel target for cancer therapy based on microtubule poisons. *Molecules* https://doi.org/10.3390/molecules21050663 (2016).
68. Hohmann, T. & Dehghani, F. The cytoskeleton—A complex interacting meshwork. *Cells* **8**, 362 (2019).
69. Seetharaman, S. & Etienne-Manneville, S. Cytoskeletal crosstalk in Cell migration. *Trends Cell Biol.* **30**, 720–735 (2020).
70. Mirossay, L., Varinská, L. & Mojžiš, J. Antiangiogenic effect of flavonoids and chalcones: An update. *Int. J. Mol. Sci.* https://doi.org/10.3390/ijms19010027 (2017).
71. Chen, Y. et al. LYG-202, a newly synthesized flavonoid, exhibits potent anti-angiogenic activity in vitro and in vivo. *J. Pharmacol. Sci.* **112**, 37–45 (2010).
72. Fan, J. & de Lannoy, I. A. M. Pharmacokinetics. *Biochem. Pharmacol.* **87**, 93–120 (2014).
73. Ferreira, L. L. G. & Andricopulo, A. D. ADMET modeling approaches in drug discovery. *Drug Discov. Today* **24**, 1157–1165 (2019).
74. Jia, C.-Y., Li, J.-Y., Hao, G.-F. & Yang, G.-F. A drug-likeness toolbox facilitates ADMET study in drug discovery. *Drug Discov. Today* **25**, 248–258 (2020).
75. Daina, A., Michielin, O. & Zoete, V. SwissADME: A free web tool to evaluate pharmacokinetics, drug-likeness and medicinal chemistry friendliness of small molecules. *Sci. Rep.* **7**, 42717. https://doi.org/10.1038/srep42717 (2017).
76. Yang, H. et al. admetSAR 2.0: Web-service for prediction and optimization of chemical ADMET properties. *Bioinformatics* **35**, 1067–1069. https://doi.org/10.1093/bioinformatics/bty707 (2019).
77. Lv, Y., Ma, X., Du, Y. & Feng, J. Understanding patterns of brain metastasis in triple-negative breast cancer and exploring potential therapeutic targets. *Onco. Targets. Ther.* **14**, 589–607. https://doi.org/10.2147/OTT.S293685 (2021).
78. Kalliokoski, A. & Niemi, M. Impact of OATP transporters on pharmacokinetics. *Br. J. Pharmacol.* **158**, 693–705 (2009).

79. Zhang, Y. & Hagenbuch, B. Protein–protein interactions of drug uptake transporters that are important for liver and kidney. *Biochem. Pharmacol.* **168**, 384–391 (2019).
80. Stipp, M. C. & Acco, A. Involvement of cytochrome P450 enzymes in inflammation and cancer: A review. *Cancer Chemother. Pharmacol.* **87**, 295–309 (2021).
81. Lipinski, C. A., Lombardo, F., Dominy, B. W. & Feeney, P. J. Experimental and computational approaches to estimate solubility and permeability in drug discovery and development settings. *Adv. Drug Deliv. Rev.* **46**, 3–26 (2001).
82. Brenk, R. et al. Lessons learnt from assembling screening libraries for drug discovery for neglected diseases. *ChemMedChem* **3**, 435–444 (2008).
83. Song, L. et al. Icariin-induced inhibition of SIRT6/NF-κB triggers redox mediated apoptosis and enhances anti-tumor immunity in triple-negative breast cancer. *Cancer Sci.* **111**, 4242–4256 (2020).
84. Pandey, N. & Black, B. E. Rapid detection and signaling of DNA damage by PARP-1. *Trends Biochem. Sci.* **46**, 744–757 (2021).
85. Luo, X. & Lee Kraus, W. On par with PARP: Cellular stress signaling through poly(ADP-ribose) and PARP-1. *Genes Dev.* **26**, 417–432 (2012).
86. Lord, C. J., Tutt, A. N. J. & Ashworth, A. Synthetic lethality and cancer therapy: Lessons learned from the development of PARP inhibitors. *Annu. Rev. Med.* **66**, 455–470 (2015).
87. Mandapati, A. & Lukong, K. E. Triple negative breast cancer: Approved treatment options and their mechanisms of action. *J. Cancer Res. Clin. Oncol.* **149**, 3701–3719 (2023).
88. Spiegel, J. O., Van Houten, B. & Durrant, J. D. PARP1: Structural insights and pharmacological targets for inhibition. *DNA Repair (Amst)* **103**, 103125 (2021).
89. Wang, Y.-Q. et al. An update on poly(ADP-ribose)polymerase-1 (PARP-1) Inhibitors: Opportunities and challenges in cancer therapy. *J. Med. Chem.* **59**, 9575–9598 (2016).
90. Slade, D. PARP and PARG inhibitors in cancer treatment. *Genes Dev.* **34**, 360–394 (2020).
91. Hartman, A.-R. et al. Prevalence of BRCA mutations in an unselected population of triple-negative breast cancer. *Cancer* **118**, 2787–2795 (2012).
92. Cardillo, T. M. et al. Synthetic lethality exploitation by an anti-trop-2-SN-38 antibody-drug conjugate, IMMU-132, plus PARP inhibitors in BRCA1/2-wild-type triple-negative breast cancer. *Clin. Cancer Res.* **23**, 3405–3415 (2017).
93. Pulliam, N. et al. An effective epigenetic-PARP inhibitor combination therapy for breast and ovarian cancers independent of BRCA mutations. *Clin. Cancer Res.* **24**, 3163–3175 (2018).
94. Carey, J. P. W. et al. Synthetic lethality of PARP inhibitors in combination with MYC blockade is independent of BRCA status in triple-negative breast cancer. *Cancer Res.* **78**, 742–757 (2018).
95. Dilmac, S. & Ozpolat, B. Mechanisms of PARP-inhibitor-resistance in BRCA-mutated breast cancer and new therapeutic approaches. *Cancers (Basel)* **15**, 3642 (2023).
96. Maluchenko, N. V., Feofanov, A. V. & Studitsky, V. M. PARP-1-associated pathological processes: Inhibition by natural polyphenols. *Int. J. Mol. Sci.* **22**, 11441 (2021).
97. Li, J. et al. A DNA-encoded library for the identification of natural product binders that modulate poly (ADP-ribose) polymerase 1, a validated anti-cancer target. *Biochem. Biophys. Res. Commun.* **533**, 241–248 (2020).
98. Slade, D. Mitotic functions of poly(ADP-ribose) polymerases. *Biochem. Pharmacol.* **167**, 33–43 (2019).
99. Chang, P., Jacobson, M. K. & Mitchison, T. J. Poly(ADP-ribose) is required for spindle assembly and structure. *Nature* **432**, 645–649 (2004).
100. Colicchia, V. et al. PARP inhibitors enhance replication stress and cause mitotic catastrophe in MYCN-dependent neuroblastoma. *Oncogene* **36**, 4682–4691 (2017).
101. Kim, M. K. Novel insight into the function of tankyrase. *Oncol. Lett.* **16**, 6895–6902 (2018).
102. Chang, P., Coughlin, M. & Mitchison, T. J. Tankyrase-1 polymerization of poly(ADP-ribose) is required for spindle structure and function. *Nat. Cell Biol.* **7**, 1133–1139 (2005).
103. Yashiroda, Y. et al. A novel yeast cell-based screen identifies flavone as a tankyrase inhibitor. *Biochem. Biophys. Res. Commun.* **394**, 569–573 (2010).
104. Yu, M., Yang, Y., Sykes, M. & Wang, S. Small-molecule inhibitors of tankyrases as prospective therapeutics for cancer. *J. Med. Chem.* **65**, 5244–5273 (2022).
105. Narwal, M. et al. Discovery of tankyrase inhibiting flavones with increased potency and isoenzyme selectivity. *J. Med. Chem.* **56**, 7880–7889 (2013).
106. Thorsell, A.-G. et al. Structural basis for potency and promiscuity in poly(ADP-ribose) polymerase (PARP) and tankyrase inhibitors. *J. Med. Chem.* **60**, 1262–1271 (2017).
107. Di Micco, S. et al. Identification by inverse virtual screening of magnolol-based scaffold as new tankyrase-2 inhibitors. *Bioorg. Med. Chem.* **26**, 3953–3957 (2018).
108. Tomassi, S. et al. From PARP1 to TNKS2 inhibition: A structure-based approach. *ACS Med. Chem. Lett.* **11**, 862–868. https://doi.org/10.1021/acsmedchemlett.9b00654 (2020).
109. Marder, M. et al. Synthesis of halogenated/nitrated flavone derivatives and evaluation of their affinity for the central benzodiazepine receptor. *Bioorganic Med. Chem. Lett.* **7**, 2003–2008 (1997).
110. Marder, M. et al. Detection of benzodiazepine receptor ligands in small libraries of flavone derivatives synthesized by solution phase combinatorial chemistry. *Biochem. Biophys. Res. Commun.* **249**, 481–485 (1998).
111. Carabias, P. et al. Galectin-1 confers resistance to doxorubicin in hepatocellular carcinoma cells through modulation of P-glycoprotein expression. *Cell Death Dis.* **13**, 79 (2022).
112. Nicoud, M. B. et al. Study of the antitumour effects and the modulation of immune response by histamine in breast cancer. *Br. J. Cancer* **122**, 348–360 (2020).
113. Ferragut, F. et al. Dual knockdown of galectin-8 and its glycosylated ligand, the activated leukocyte cell adhesion molecule (ALCAM/CD166), synergistically delays in vivo breast cancer growth. *Biochim. Biophys. Acta Mol. Cell Res.* **1866**, 1338–1352 (2019).
114. Filimonov, D. A. et al. Prediction of the biological activity spectra of organic compounds using the pass online web resource. *Chem. Heterocycl. Compd.* **50**, 444–457 (2014).
115. Daina, A., Michielin, O. & Zoete, V. SwissTargetPrediction: Updated data and new features for efficient prediction of protein targets of small molecules. *Nucleic Acids Res.* **47**, W357–W364 (2019).
116. Yao, Z.-J. et al. TargetNet: A web service for predicting potential drug-target interaction profiling via multi-target SAR models. *J. Comput. Aided. Mol. Des.* **30**, 413–424 (2016).
117. Lee, K., Lee, M. & Kim, D. Utilizing random Forest QSAR models with optimized parameters for target identification and its application to target-fishing server. *BMC Bioinf.* **18**, 567. https://doi.org/10.1186/s12859-017-1960-x (2017).
118. Keiser, M. J. et al. Relating protein pharmacology by ligand chemistry. *Nat. Biotechnol.* **25**, 197–206 (2007).
119. Nickel, J. et al. SuperPred: Update on drug classification and target prediction. *Nucleic Acids Res.* **42**, W26-31 (2014).
120. Molecular Operating Environment (MOE) 2024 Chemical Computing Group ULC. 910–1010 at https://www.chemcomp.com (2024).
121. Santi, M. D. et al. Xanthine oxidase inhibitory activity of natural and hemisynthetic flavonoids from *Gardenia oudiepe* (Rubiaceae) in vitro and molecular docking studies. *Eur. J. Med. Chem.* **143**, 577–582 (2018).

122. Peralta, M. A., Santi, M. D., Cabrera, J. L. & Ortega, M. G. Dalea genus, chemistry, and bioactivity studies. In: *Studies in Natural Products Chemistry* (ed. Atta-ur-Rahman, B. T.-S. in N. P. C.) vol. 62 307–341 (Elsevier, 2019).
123. Carvalho, D. et al. Structural evidence of quercetin multi-target bioactivity: A reverse virtual screening strategy. *Eur. J. Pharm. Sci.* **106**, 393–403 (2017).
124. Wang, E. et al. End-point binding free energy calculation with MM/PBSA and MM/GBSA: Strategies and applications in drug design. *Chem. Rev.* **119**, 9478–9508 (2019).

Acknowledgements

V.S.V. and M.B.N. are fellows from Consejo Nacional de Investigaciones Científicas y Técnicas (CONICET). V.C.B., M.M., M.G.O., V.A.M., M.T.E. and M.F.T. are researchers from CONICET. We thank Magalí C. Cercato for histological technical assistance.

Author contributions

V.S.V. performed most of the experiments and analyzed the results. V.B., M.B.N., M.B. and V.A.M. performed experiments and contributed with data analysis. M.M. synthesized 2'NF and contributed with data analysis. J.C., M.P.Z. and M.G.O carried out Molecular docking and dynamics studies. S.V. examined all histological samples. M.T.E. and M.F.T. designed the study, analyzed the results, and wrote the paper. All authors read and approved the final manuscript.

Funding

This work was supported by PUE 046-CONICET, awarded to IQUIFIB-CONICET.

Declarations

Conflict of interest

The authors declare that they have no conflict of interest.

Additional information

Supplementary Information The online version contains supplementary material available at https://doi.org/10.1038/s41598-025-34214-w.

Correspondence and requests for materials should be addressed to M.F.T.

Reprints and permissions information is available at www.nature.com/reprints.

Publisher's note Springer Nature remains neutral with regard to jurisdictional claims in published maps and institutional affiliations.